Element Abundances of Evolved Stars in the Galactic Globular Cluster M5

A thesis submitted to The University of Manchester for the degree of
Master of Science by Research
in the Faculty of Engineering and Physical Sciences

2015

Karthigeyan Ramesh Kumar
School of Physics and Astronomy

Contents

List of Figures **7**

List of Tables **9**

Abstract **11**

Declaration **12**

Copyright Statement **13**

Acknowledgements **14**

The Author **15**

List of Abbreviations and Symbols **16**

1 Introduction **19**

1.1 Motivation 19

1.2 Globular Clusters 20

1.2.1 Historical Significance 20

1.2.2 Cluster Environment 21

1.2.3 Metallicity and Cluster Age 22

1.2.4 Formation Models 23

1.3 Chemical Enrichment 25

1.3.1 Stellar Evolution 25

1.3.2 Abundance Patterns 28
1.4 M5 30
1.5 Overview of this thesis 31

2 Analysis Method **35**
2.1 Observation Data 35
2.2 Equivalent Width Measurement 35
2.3 Stellar Parameters 42
2.3.1 Model Atmospheres 43
2.3.2 Abundance dependance with stellar parameters 43
2.3.3 Stellar Parameters 45

3 Results **51**
3.1 Silicon 52
3.2 Calcium 53
3.3 Titanium 53
3.4 α Elements 55
3.5 Chromium 55
3.6 Yittrium 56
3.7 Cerium 56
3.8 Neodymium 58
3.9 Erbium 58
3.10 Summary 60

4 Error Analysis **67**
4.1 Measurement Error 67
4.2 Error due to Stellar Parameter Uncertainty 69

5 Discussion **75**
5.1 Variation of [Fe/H] with Stellar Parameters 75

5.2 Determining the correctness of model atmospheres using Titanium abundance 77
5.3 Variation of abundance with radial distance 78
5.4 Comparison with photometry 83
5.5 Variation between AGB and RGB star mass 89

6 Conclusion **93**

References **96**

List of Figures

1 Optical telescope used by the author for this work 16

1.1 Positions of known Galactic globular clusters 20
1.2 Bimodal distribution of metallicity in Milky Way globular cluster . . . 23
1.3 HRD of a Sun-like star 25
1.4 The CMD of ω Centauri from the work of Bedin et al. (2004) 29
1.5 CMD of the cluster M5 31

2.1 Pictorial definition of equivalent width. 36
2.2 EW measurement software interface 37
2.3 MOOG output graphs 44
2.4 A schematic representation of the analysis procedure followed. 46

3.1 Plot of [Si/Fe] versus [Fe/H] with a linear fit. 52
3.2 Plot of [Ca/Fe] versus [Fe/H] with a linear fit. 53
3.3 Plot of [Ti I/Fe] versus [Fe/H] with a linear fit. 54
3.4 Plot of [Ti II/Fe] versus [Fe/H] with a linear fit. 55
3.5 Plot of [α/Fe] versus [Fe/H] with a linear fit. 56
3.6 Plot of [Cr/Fe] versus [Fe/H] with a linear fit. 57
3.7 Plot of [Y/Fe] versus [Fe/H] with a linear fit. 57
3.8 Plot of [Ce/Fe] versus [Fe/H] with a linear fit. 58
3.9 Plot of [Nd/Fe] versus [Fe/H] with a linear fit. 59
3.10 Plot of [Er/Fe] versus [Fe/H] with a linear fit. 59

4.1 Plot showing variation of [Fe/H] with SNR 68

5.1 Plot of [Fe/H] versus T_{eff} with a linear fit. 76
5.2 Plot of [Fe/H] versus log(g) with a linear fit. 76
5.3 Plot of [Ti II/Ti I] versus [Ti I/Fe] with a linear fit. 77
5.4 Plot of [Ti I/Ti II] versus T_{eff} 78
5.5 Histogram showing distribution of projected distances from the cluster centre 79
5.6 Plot of [Fe/H] versus projected distance from cluster centre with a linear fit. 80
5.7 Plot of [Si/Fe] versus projected distance from cluster centre with a linear fit. 80
5.8 Plot of [Ca/Fe] versus distance from cluster centre with a linear fit. . . 81
5.9 Plot of [Ti I/Fe] versus projected distance from cluster centre with a linear fit. 82
5.10 Plot of [Ti II/Fe] versus distance from cluster centre with a linear fit. . 82
5.11 Plot of [α/H] versus distance from cluster centre with a linear fit. . . . 83
5.12 Plot of [Cr/Fe] versus distance from cluster centre with a linear fit. . . 84
5.13 Plot of [Y II/Fe] versus distance from cluster centre with a linear fit. . 84
5.14 Plot of [Ce II/Fe] versus distance from cluster centre with a linear fit. . 85
5.15 Plot of [Nd II/Fe] versus distance from cluster centre with a linear fit. 85
5.16 Plot of [Er II/Fe] versus distance from cluster centre with a linear fit. . 86
5.17 CMD of sample stars. RGB star are represented by red while AGB stars are represented by green. 91
5.18 Variation of derived mass for RGB (red) and AGB (green) 91

List of Tables

1.1 Typical parameters of globular and open clusters 21
1.2 Abundance studies on M5 32

2.1 Linelist used in this study 38
2.2 Stellar parameter result summary 47

3.1 Comparison between average [Fe/H] values 51
3.2 The comparison of the stellar parameters in this study with literature values 61
3.3 Measured element abundances 62

4.1 σ_{meas} for the measured lines 68
4.2 Uncertainties due to stellar parameters 70
4.4 Signal-to-noise ratio seen in the OB26 setting (λ 6627Å) for the observed stars 70
4.3 Comparison of abundance dependencies with stellar parameter between Ivans et al. (2001) (1) and this work (2) with errors recomputed using the same perturbation step for comparison purpose only. 74

5.1 Comparison between photometric and spectroscopic temperatures . . 87

6.1 Average values of [X/Fe] found in this study 94

The University of Manchester

ABSTRACT OF THESIS submitted by Karthigeyan Ramesh Kumar
for the Degree of Master of Science by Research and entitled
A Study of Element Abundances of Evolved Stars in the Galactic Globular Cluster M5.
2015.

I present the iron abundance and abundance ratios for 9 elements: Si I, Ca I, Ti I and Ti II, Cr I, Y II, Ce II, Nd II and Er II with respect to Fe in a sample of 55 stars along the RGB and AGB of the globular cluster M5. The spectra were obtained using the Hectochelle spectrograph at the Multiple Mirror Telescope. The spectral coverage was from 5070 Å to 5390 Å, 6010 Å to 6510 Å and 6391 Å to 6873 Å.

An average iron abundance [Fe/H]=-1.29 ± 0.15 dex was found, consistent with Harris (2010). The cluster averages of [Si/Fe], [Ca/Fe], [Ti I/Fe], [Ti II/Fe], [Cr/Fe], [Ce/Fe], [Nd/Fe] and [Er/Fe] are 0.16 ± 0.17, 0.13 ± 0.12, 0.4 ± 0.15, 0.31 ± 0.13, 0.10 ± 0.41, 0.01 ± 0.16, 0.13 ± 0.13, 0.52 ± 0.14, 1.27 ± 0.18 dex, respectively. The [Ti II/Fe] matches the literature value. The [Si I/Fe] and [Ca/Fe] are found to be lower than the reported values while the other elements of this study show a higher abundance.An anti-correlation is found between the abundance ratios and the iron abundance which can be explained due to an artificially high spread in [Fe/H]. The combined behaviour of α-elements is also studied and we report an enhancement of α-elements relative to iron seen in this cluster. The abundance variations do not show any trend with the distance from the cluster centre. The obtained spectroscopic temperatures are found to match the photometric temperatures within the error margins except for three stars. An attempt is made to differentiate the RGB and AGB stars using their derived masses. The systematic offset in ΔT_{eff} between RGB and AGB prevents us from accurately calculating the mass loss in the RGB.

Declaration

I declare that no portion of the work referred to in the thesis has been submitted in support of an application for another degree or qualification of this or any other university or other institute of learning.

Copyright Statement

(i) The author of this thesis (including any appendices and/or schedules to this thesis) owns certain copyright or related rights in it (the "Copyright") and s/he has given The University of Manchester certain rights to use such Copyright, including for administrative purposes.

(ii) Copies of this thesis, either in full or in extracts and whether in hard or electronic copy, may be made only in accordance with the Copyright, Designs and Patents Act 1988 (as amended) and regulations issued under it or, where appropriate, in accordance with licensing agreements which the University has from time to time. This page must form part of any such copies made.

(iii) The ownership of certain Copyright, patents, designs, trade marks and other intellectual property (the "Intellectual Property") and any reproductions of copyright works in the thesis, for example graphs and tables ("Reproductions"), which may be described in this thesis, may not be owned by the author and may be owned by third parties. Such Intellectual Property and Reproductions cannot and must not be made available for use without the prior written permission of the owner(s) of the relevant Intellectual Property and/or Reproductions.

(iv) Further information on the conditions under which disclosure, publication and commercialisation of this thesis, the Copyright and any Intellectual Property and/or Reproductions described in it may take place is available in the University IP Policy (see http://www.campus.manchester.ac.uk/medialibrary/policies/intellectual-property.pdf), in any relevant Thesis restriction declarations deposited in the University Library, The University Library's regulations (see http://www.manchester.ac.uk/library/aboutus/regulations) and in The University's policy on presentation of Theses.

Acknowledgements

I would like to thank my supervisor, Iain McDonald, for all his help and support throughout this year. I would also like to thank Christian Johnson and Albert Zijlstra for their invaluable guidance. I would also like to thank my parents and my sister for their support. I am greatly endebted to the various PhD and Masters students who have helped me on my way; in particular Skandar Taj for his help with equivalent width measurements, and Evan Eames and Shweta Agarwal for welcoming me and making the office a fun place to be.

This thesis was typeset with LaTeX.

The Author

The author graduated from the Indian Institute of Technology Guwahati in 2013 with a B.Tech in Engineering Physics. Since 2014 he has been studying for an MSc by Research in Astronomy and Astrophysics at the Jodrell Bank Centre for Astrophysics. The results of this research are presented in this thesis.

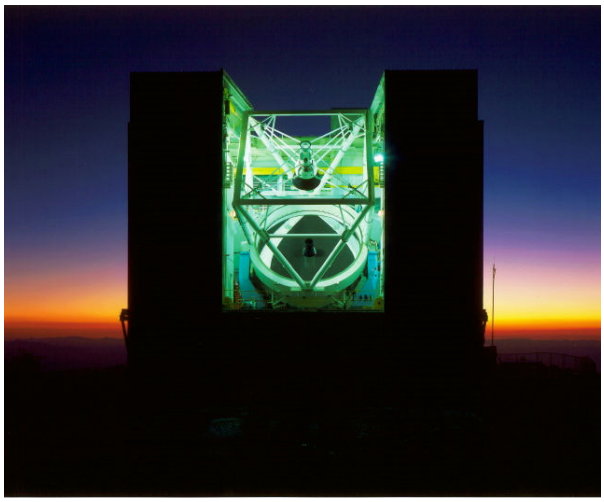

Figure 1: The MMT opticaltelescope in Arizona which was used to collect the stellar spectra used in this work.Source:`www.mmto.org`

List of Abbreviations and Symbols

The following abbreviations and symbols are used throughout this thesis:

1D – One Dimensional

AGB – Asymptotic Giant Branch

CMD – Colour–Magnitude Diagram

CNO – Carbon-Nitrogen-Oxygen

CWL – Centre Wavelength

E.P. – Excitation Potential

EW – Equivalent Width

FWHM – Full Width at Half Maximum

HRD – Hertzsprung-Russell diagram

HB – Horizontal Branch

ISM – Interstellar Medium

$L_{\odot}$ – Solar Luminosity

LMC – Large Magellanic CLoud

LTE − Local Thermodynamic Equilibrium

$M_{\odot}$ − Solar Mass

MSTO − Main Sequence Turn Off

MMT − Multiple Mirror Telescope

RGB − Red Giant Branch

rms − root mean square

SAO − Smithsonian Astrophysical Observatory

1

Introduction

1.1 Motivation

Recent studies of globular clusters suggest that they contain multiple generations of star formation, e.g. D'Ercole et al. (2008), Carretta et al. (2009b), Dalessandro et al. (2014), etc. Here, I will study the chemical composition of evolved stars in the globular cluster M5. This knowledge could then help us understand the cluster's formation and the chemical enrichment of the galaxy. We are also interested in testing whether there are any chemical differences between stars on the red giant branch (RGB) and stars on the asymptotic giant branch (AGB) on the Hertzsprung-Russell diagram (HRD).
Recent conflicting reports argue about the evolution of the second generation of stars. Campbell et al. (2013) observed the absence of second-generation AGB stars in NGC 6752 while Johnson et al. (2015) observed their presence in 47 Tuc. M5, having a metallicity between these two clusters and a well separated RGB and AGB, is ideal for testing stellar evolutionary models.

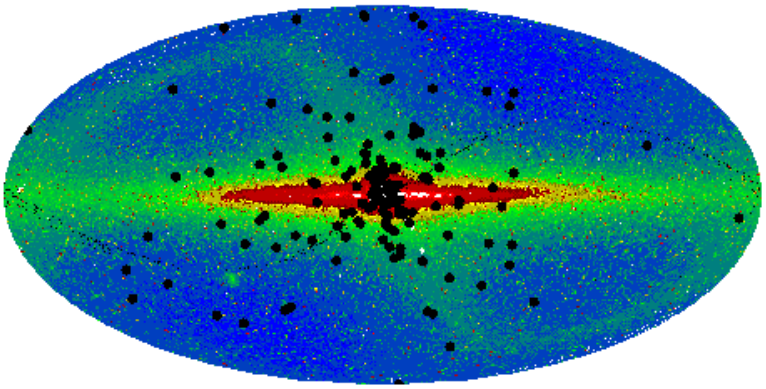

Figure 1.1: The positions of the known Galactic globular clusters are plotted as black circles on top of the COBE FIRAS 2.2-μm map of the Galaxy using a Mollweide projection. Image source URL: `http://www.dartmouth.edu/~chaboyer/mwgc.html`

1.2 Globular Clusters

1.2.1 Historical Significance

Globular clusters were some of the first objects to be observed with the telescope. The first globular cluster, M22, was discovered in 1665 by Johann Abraham Ihle, a German amateur astronomer (Jones 1991). However it was not until 1789 that William Herschel coined the term globular cluster for such objects in his catalogue of deep sky objects, due to their spherical shape. Many more clusters were discovered subsequently and in the 1830s John Herschel noticed that these clusters tend to occur more in the direction of Sagittarius (Ashman and Zepf 1998). This fact was later used by Shapley, in 1918, to estimate distance of the Solar System from the Galactic Centre with Sagittarius marking the direction. Presently, there are around 157 globular clusters identified in the Milky Way galaxy (Harris 2010). Their distribution is showed in Figure 1.1.

Table 1.1: Typical parameters of globular and open clusters

	Globular	Open
Central density, ρ_0	1×10^4 $M_\odot$ pc^{-3}	10 $M_\odot$ pc^{-3}
Core radius, r_c	1 pc	1 pc
Half-mass radius, r_h	3 pc	2 pc
Tidal radius, r_t	35 pc	10 pc
Central velocity dispersion, σ_0	6 km s^{-1}	0.3 km s^{-1}
Crossing time (line-of-sight), r_h/σ_0	0.5 Myr	7 Myr
Mass-to-light ratio, Υ_R	$2\Upsilon_\odot$	$1\Upsilon_\odot$
Mass	2×10^5 $M_\odot$	$3 \times 10^2 M_\odot$
Number in Galaxy	150	10^5

1.2.2 Cluster Environment

Globular clusters are typically large, compact, spherical star clusters in the outer regions of a galaxy away from the galactic disk. They contain around $10^4 - 10^6$ stars with varying degrees of central condensation. Due to the presence of a stellar density gradient, globular clusters have different radii measurements associated with them, including: the core radius (r_c) where the surface brightness has fallen to half the central value, the half-light radius (r_h) which contains half of the total luminosity and the tidal radius (r_t) which marks the radius at which the galaxy's gravity dominates over the cluster's (Binney and Tremaine 1987). Most of the Galactic globular clusters orbit the Galaxy about the Galactic centre, in orbits not usually lying in the galactic plane, in random orientations. This feature distinguishes them from the open clusters found in the spiral arms of the Milky Way which participate in the Galactic rotation. Also, globular clusters tend to contain old, metal-poor stars while the stars in the galactic disk tend to be metal-rich stars like the Sun. The typical values of some of the parameters for globular and open clusters of the Milky Way galaxy are tabulated in Table 1.1, reproduced from Binney and Tremaine 1987.

1.2.3 Metallicity and Cluster Age

Being simple stellar systems, composed of low metallicity Population II stars leads us to believe that globular clusters are very old objects. The present Universe is thought to be filled by stars of three generations namely, Population III, II, and I, with the oldest (Population III) stars consisting only of hydrogen and helium (first stars to form after Big Bang nucleosynthesis). Population II stars are the metal-poor stars formed from the ejecta of the previous generation of stars while Population I stars are the metal-rich stars like the Sun. The metallicity of a star, Z, is defined as the mass fraction of all elements heavier than helium. It is often convenient to express it using the easily observable quantity of iron abundance, [Fe/H],

$$[\mathrm{Fe/H}] = log_{10}\left(\frac{N_{Fe}}{N_H}\right)_{star} - log_{10}\left(\frac{N_{Fe}}{N_H}\right)_{sun} \tag{1.1}$$

where N_{Fe} and N_H represent the number of iron and hydrogen atoms per unit volume, respectively. According to Beers and Christlieb (2005), a star is considered "very metal poor" if it has [Fe/H]< -2.0 and "metal poor" if it has [Fe/H]< -1.0. The majority of the stars in Galactic globular clusters show a homogeneity in the iron-peak (Fe, V, Cr, Mn, Co and Ni) element abundances (Suntzeff 1993; Carretta et al. 2009a) so that [Fe/H] of the overall cluster can be determined by taking a few samples of the constituent cluster stars. The [Fe/H] distribution of Milky Way globular clusters shows a bimodal distribution (as illustrated in Figure 1.2) with [Fe/H] peaks at -1.59 and -0.51 dex, corresponding dispersions of 0.34 and 0.23 dex, respectively (Ashman and Zepf 1998). We categorize the two distinct populations as halo clusters and thick-disk clusters, respectively. The thick-disk clusters have a flattened spatial distribution and rotate about the Galactic Center while the halo clusters have little net rotation and spherical distribution. The bimodal metallicity distribution is seen in globular clusters of almost all massive galaxies (Brodie and Strader 2006).

The metal-poor stars found in the globular clusters previously helped to determine a lower limit to the age of the Universe. Ages are generally determined by fitting stellar models to the observed Hertzsprung-Russell diagram of the cluster. Carretta

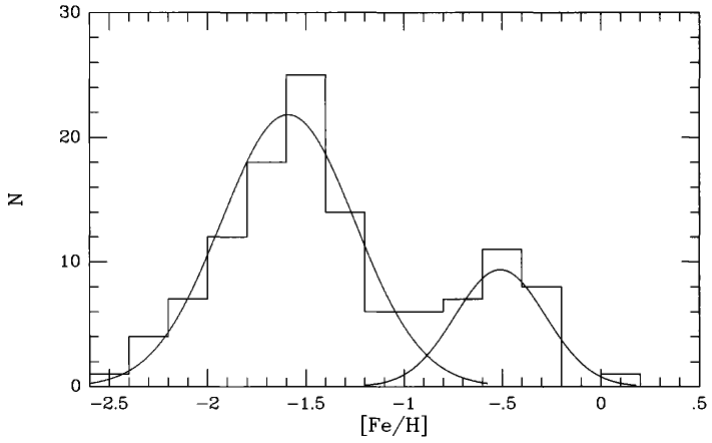

Figure 1.2: The metallicity distribution of Milky Way globular clusters. Also shown are the individual Gaussian fits to the two populations. Image taken from Ashman and Zepf (1998)

et al. (2000) derives the average age of Milky Way globular clusters as 12.9 ± 2.9 Gyr by fitting stellar evolution models to brown dwarfs. Contrastingly, intermediate-age (1-3 Gyrs old) globular clusters have been found in the LMC (see Milone et al. (2009) and references therein). Also, galaxy mergers like the Antennae show young, protoglobular, cloud like objects (Eggers et al. 2005). Hence Milky Way globular clusters can be used to trace its past merger events.

1.2.4 Formation Models

The formation process of globular clusters is not fully understood and remains an open problem in astrophysics. Many theories and models have been put forward which explain the variation of a particular property of clusters but no single theory exists which adequately explains the formation and variation of all the observed properties in a general globular cluster. According to Fall and Rees (1988), these theories can broadly be classified as primary, secondary and tertiary depending on when the clusters formed with respect to the galaxy. Some of these models are discussed as follows.

The primary models suggest the formation of globular clusters before the formation of

the galaxy using a hierarchical clustering model (Peebles and Dicke 1968). Although these models explain the globular cluster luminosity functions (defined as the number of stars in that cluster per unit magnitude) which are observed to be independent of parent galaxy type, they fail to explain the spatial distribution, number, and metallicity of the clusters, which are dependent on the host galaxy (Ashman and Zepf 1998). Also the similarity between stars in the galactic bulge and the thick-disk clusters provide evidence that these clusters could not have formed before the host galaxy.

Secondary formation models suggest globular clusters form contemporaneously to the Galaxy's formation. This is the scenario which has wide acceptance among the researchers in this field due to the presence of a galactocentric gradient in the metallicity of Milky Way globulars (Pilachowski 1984), which provides evidence for the participation of globular clusters in the collapse of the protogalactic cloud. One such model proposed by Fall and Rees (1985) suggests that thermal instabilities in the protogalactic medium lead to the formation of cool gas clouds in pressure equilibrium with the surrounding hot gas. These cool clouds, being of similar mass to the globular clusters ($\backsim 10^6 M_\odot$), are identified to be their progenitors. However, the requirement by this model for the cool clouds to maintain a temperature of 10^4 K poses problems. Although this model explains the formation of low metallicity halo clusters adequately it is unable to explain the thick-disk clusters which show higher metal content. Most secondary models also fail in explaining the bimodal distribution seen in the metallicity of the globular clusters.

This leads us to the tertiary models which suggest the formation of globular clusters after the formation of the galaxy. Burkert et al. (1992) proposes that thick-disk globulars are formed in an intermediate step in the collapse of the galactic spheroid to a thin disk. While this may be true, Zinnecker et al. (1988) suggests that globular clusters are the cores of nucleated dwarf ellipticals after their accretion to the host galaxy. This model was proposed after observing certain similarities between the globular clusters and the dense nucleus of dwarf ellipticals. However this model is not able to explain the observed correlations of cluster properties with galactocentric distance and differ-

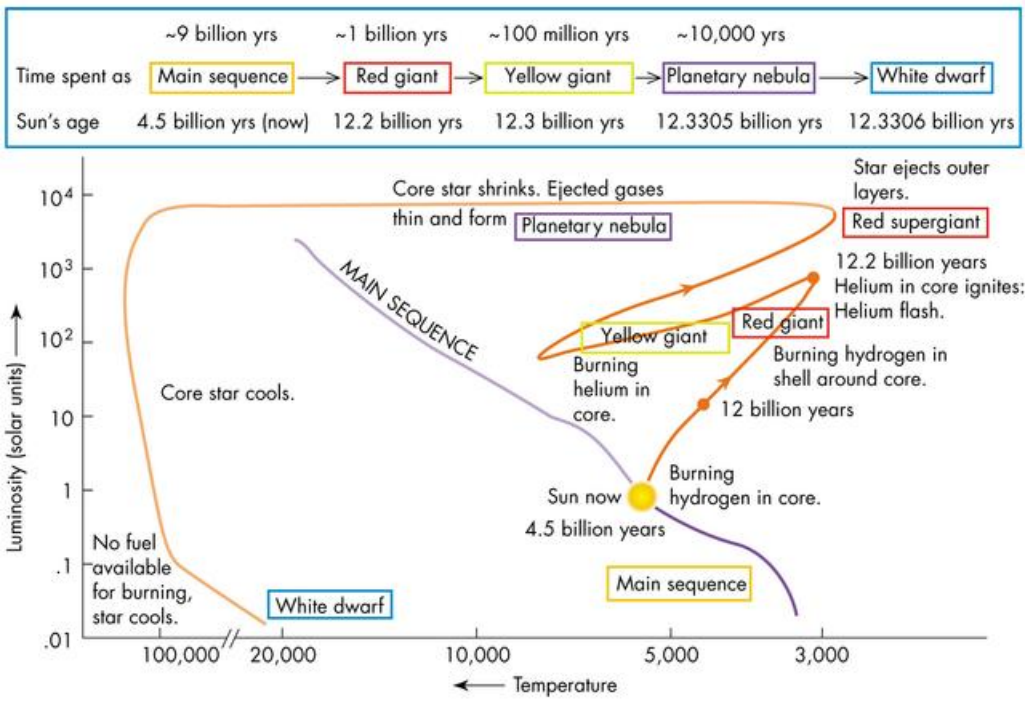

Figure 1.3: Stellar evolution of a sun like star. Note that the majority of its life time is spent on the main sequence. Image Source URL:`http://www.profjohn.com/courses/ast1004/starlives/starlives.htm`

ences in the masses between dwarf elliptical nuclei and globular clusters. Also young proto-globular clusters in interacting merger systems (Eggers et al. 2005) provide some evidence for the tertiary models.

1.3 Chemical Enrichment

1.3.1 Stellar Evolution

On large time scales ($\backsim 10^8$ yrs) the passage of the cluster through the galactic disk should sweep out most of the intracluster medium from the globular clusters (Spergel 1991) while on short time scales UV radiation from white dwarfs are efficient in expelling the gas medium (McDonald and Zijlstra 2015a). The tenuous gas medium in

globular clusters is not sufficient to form molecular clouds hence star formation has ceased and evolved stars are the only observable objects in the globular clusters. Although the [Fe/H] value remains the same among the stars in a globular cluster, there are large variations seen in the abundances of light elements: C, N, O, Na and Al within a cluster (Suntzeff 1993) which could be explained by taking a closer look at stellar evolution. Stellar evolution can be traced with the help of the Hertzsprung-Russell (HR) diagram (see Figure 1.3) which is a scatter plot of stellar luminosities against surface temperature.

Star formation begins with the gravitational collapse of molecular clouds where half of the gravitational energy released is lost as radiation and the other half heats up the cloud (Phillips 1999). This is called the protostar. The collapse of the protostar continues until the conditions in the core are favourable for hydrogen fusion to occur. The star enters the main-sequence phase when the hydrogen burning starts in the core and the star attains a hydrostatic equilibrium between gravity and radiation. The mass of the star greatly affects its evolution. Stars of mass less than $1.5M_{\odot}$ (3×10^{30} kg) fuse hydrogen to form helium via the proton-proton (p-p) chain. Heavier stars also fuse hydrogen via the carbon-nitrogen-oxygen (CNO) cycle. Stars spend most of their lifetime in the main sequence, however heavier stars evolve faster as they are more efficient at hydrogen burning. Hence, most of the stars observed today in globular clusters are low-mass ($\backsim 0.8M_{\odot}$), main-sequence stars.

Towards the end of the main sequence (MSTO), the star depletes the hydrogen in its core and hydrogen fusion occurs in a shell around the inert helium core. This changes the equilibrium between radiation pressure and gravity. Thus the star increases its luminosity and cools the surface temperature by expansion of its stellar atmosphere. The star now enters the red giant branch (RGB) phase. The expanding envelope becomes more convective and brings the products of hydrogen fusion up to the surface through deep convective mixing. This is also known as the first dredge-up (FDU). As a consequence this deep mixing would change the light element abundance in the stellar atmosphere.

The core temperature of an RGB star continues to increase due to the gravitational contraction of helium from hydrogen shell fusion. When the core temperature reaches $\backsim 10^8$ K helium ignites and fuses rapidly via the triple-α process to form carbon. This is called helium flash and it rapidly increases the core temperature. The carbon in the core could further react with another alpha particle to form oxygen. This process is essential in producing light elements (Li, O, Na, Si, Al, Mg) in stellar cores. The helium fusion expands the stellar core and the overlying layer which causes the hydrogen burning to decrease. The decreased energy output causes the star to contract thereby increasing its surface temperature as the star proceeds onto the horizontal branch (HB) phase. Similar to the previous hydrogen-burning phase, the HB star exhausts the helium in its core and starts fusing the helium in a shell around the carbon and oxygen core. The star then enters the asymptotic giant branch (AGB) phase. Similar to the FDU, a second dredge up occurs when the core is depleted of helium for stars with masses of $4-8$ $M_\odot$. The AGB phase is characterized with more energy output and it asymptotically approaches the RGB in colour-magnitude diagrams. This poses difficulty in distinguishing bright AGB and RGB stars near the RGB tip. Also the outer, hydrogen-burning shell periodically deposits helium into the helium-burning shell and thus causes temporary brightness of the star. This is called as thermal pulsation. This is seen in evolved AGB stars. Additionally, these pulses also help in mixing the intershell regions. These pulsations and the dredge-ups help in bringing the core nuclear fusion products towards the surface. This material is typically carbon rich and forms a carbon star when C/O$>$ 1. However, in globular clusters the stars don't normally experience enough dredge-up for this to happen.

If the mass of the star is approximately $\lesssim 8$ $M_\odot$ then it will not be able to fuse the carbon in its core. The outer layers of such a star will be ejected by stellar winds and form a planetary nebula, while the inert $C-O$ core cools and forms a white dwarf. For massive stars the core becomes hot enough to continue nuclear fusion of heavier elements. Consequently the star develops an onion-like structure with the outer layer containing

hydrogen and the inner core made of iron. Nuclear fusion stops at Fe^{56} beyond which the process becomes endothermic.

Elements heavier than iron are formed by the 'r-' (rapid) and 's-' (slow) neutron capture processes. In the s-process, the atom has enough time to β-decay to a lower atomic number. This happens in massive AGB stars. The r-process primarily happens in Type II supernovae where the neutron capture element does not have enough time to β-decay before capturing another neutron. If the mass of the stellar core is less than $\approx 1.4 M_{\odot}$ (the Chandresekar limit), it will form a white dwarf. Otherwise for heavier cores, the electron degeneracy pressure will not be able to support the gravitational collapse of the star, which will leave behind a neutron star or a black hole after undergoing a supernova. Thus the metals (elements heavier than H, He), blown out to the ISM by the supernova explosion, are recycled and seed the formation of the next generation of stars.

1.3.2 Abundance Patterns

The abundance of elements in stars is mainly found by equivalent width measurement. In this method, a profile (Voigt/Gaussian/Lorentzian) is fitted to an absorption line seen in the star and its normalised area is measured. This is then used in conjunction with local-thermodynamic-equilibrium (LTE) models of stellar atmospheres to determine the element's abundance. The other common method is the spectral synthesis method where radiative equations are solved to generate a model, which can be compared to the observed spectrum. Due to the relatively low metal content and simple spectra seen for stars in globular clusters, the equivalent width method is preferred.
The abundance of iron-peak elements is observed to be same through out the stars in a globular cluster which led to idea that all stars were formed simultaneously (Ashman and Zepf 1998). Also the narrowness of the principle sequences in the observed HRDs of globular clusters were a further proof of their homogeneity. However, inhomogene-

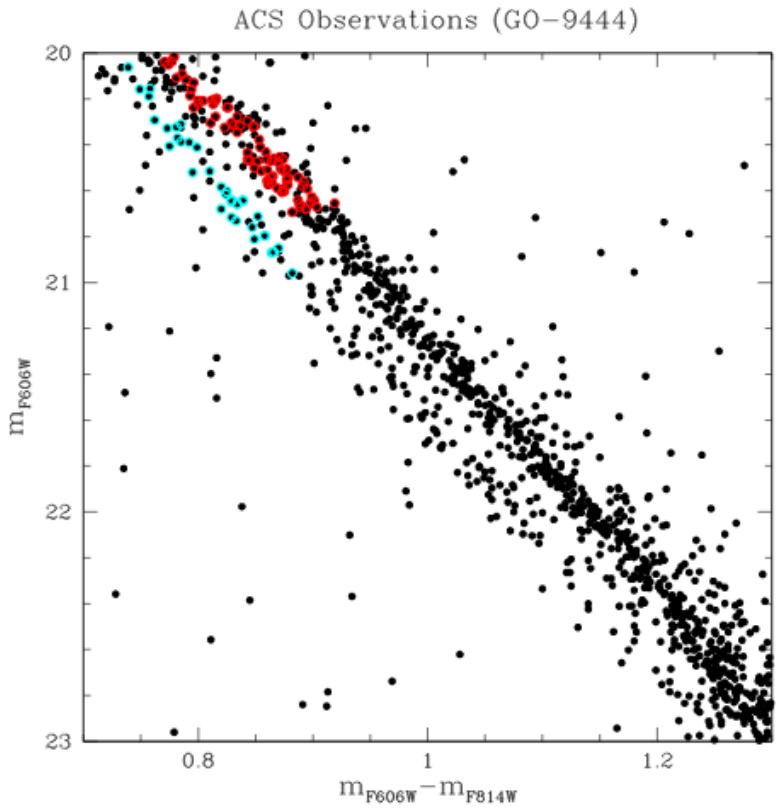

Figure 1.4: The CMD of ω Centauri from the work of Bedin et al. (2004)

ity in the light element abundances were noticed by Cohen (1978); Norris et al. (1981); Suntzeff (1993)

Initially two clusters, ω Centauri and M22, were found to show an inhomogeneity in [Fe/H] (Gratton 1982). Norris et al. (1981) found bimodality in the distribution of CN abundance of stars in NGC6752. Cohen (1978) observed the difference in Al abundance and the anti-correlation between [Na/Fe] and [O/Fe]. Shetrone (1996) also observed an anti- correlation between [Mg/Fe] and [Al/Fe].

Denissenkov et al. (1998) explains the abundance differences on the basis of either an evolutionary scenario or a primordial scenario. The evolutionary scenario proposes that the differences are a feature of deep mixing in evolved stars while the primordial scenario attributes them to chemical enrichment from a previous generation of stars. Due to instrumental limitations, abundance measurements are usually taken only for

the evolved stars in a cluster. However, Gratton et al. (2001) were able to detect the the Na-O anti-correlation in the main-sequence stars of NGC6752, thereby giving proof of the primordial scenario. They also confirmed the Mg-Al anti-correlation.
Bedin et al. (2004) discovered the presence of two main sequence, with unique turn-off points, and two subgiant branches in the colour-magnitude diagram of ω Centauri using the Hubble Space Telescope. The follow-up spectroscopic studies of the stars in the two main sequences revealed that the less-populated blue main sequence (bMS) had a higher metal content than the red main sequence (rMS). This further advanced the proposition of enrichment by multiple generations of star formation. More recently, Piotto et al. (2007) discovered a triple main sequence in NGC2808. Also, due to better resolution of the cameras, multiple sequences of RGBs are also observed (NGC362: Carretta et al. (2013); NGC1851: Milone et al. (2008)). The abundance patterns seen in globular clusters are usually taken as an indication that a second generation of stars has been enriched by material ejected by 5−8 $M_\odot$ stars because they are rich in s-process elements compared to the first generation. However both populations' chemical abundance patterns reflect those of Type II supernovae ejecta (high [α/Fe] ratios).

1.4 M5

Messier 5 (alternatively NGC 5904) is a globular cluster located in the constellation of Serpens (Dreyer 1888). The cluster is 6.2 kpc from the galactic centre, and has galactic co-ordinates of $l = 3.86$, $b = 46.80$ (Harris 2010). There are no peculiarities (presence of double or splitting of the evolution branches) seen in the CMD of M5. M5 shows a clear separation between the AGB and RGB in its CMD. The horizontal branch morphology of M5 is interesting, as it shows a wide spread in HB colour, which can be traced to a spread in HB mass (Gratton et al. 2010a). The earlier abundance measurements on M5 are tabulated in Table 1.2. Ivans et al. (2001) shows a correlation between the abundances of elements sensitive to proton capture (O, Na, Al) and CN band strength index S(3839) in M5 and an over-abundance of α−elements with respect

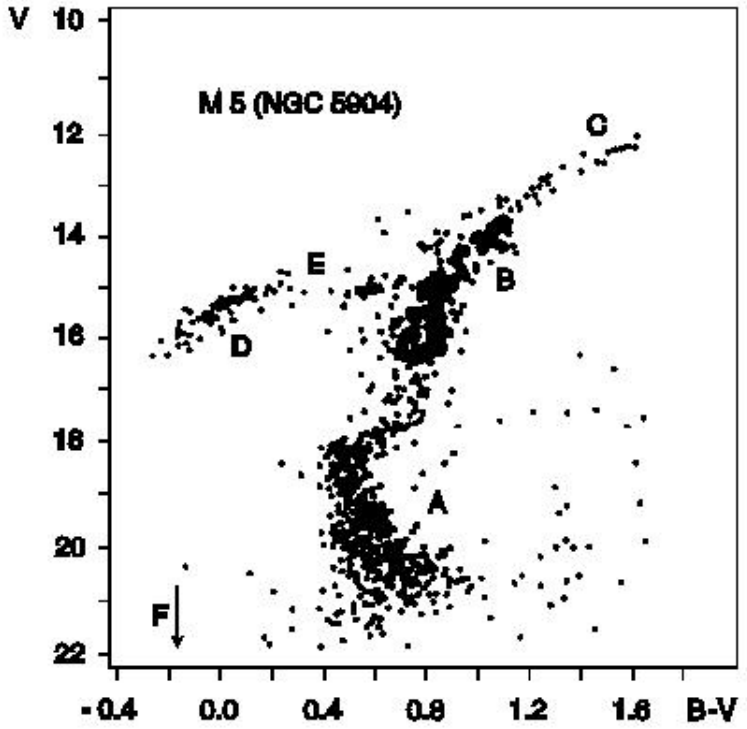

Figure 1.5: Colour–magnitude diagram of the cluster M5 where the different phases are denoted by letters A through F. A: Main sequence, B: Red Giant Branch, C: Helium Flash (RGB tip), D: Horizontal Branch (HB), E: Schwarzchild space in HB, F: White Dwarfs (below the arrow). Image Source URL: `http://messier.seds.org/xtra/leos/M005Leos.html`

to [Fe/H]. Lai et al. (2011) found the abundances of 31 elements in 17 stars of M5. Carretta et al. (2009b) performed a wider study on the Na−O anti-correlation and finds it in M5 using 136 stars.

1.5 Overview of this thesis

This thesis is organised into six chapters. Chapter 2 describes the analysis method used to determine the stellar parameters and the chemical abundance along with a brief description of the softwares used. Chapter 3 tabulates the chemical abundance results

Table 1.2: Abundance studies on M5. Note that the iron abundances are given relative to hydrogen

Species	<[X/Fe]>		
	Lai et al. (2011)	Ivans et al. (2001)	Ramírez and Cohen (2003)
Fe I	−1.51 ± 0.14	−1.30 ± 0.02	−1.34 ± 0.01
Fe II	−1.42 ± 0.09	−1.28 ± 0.02	−1.21 ± 0.01
O I	0.31 ± 0.22	0.26 ± 0.03	0.02 ± 0.04
Na I	0.19 ± 0.21	0.08 ± 0.05	0.11 ± 0.03
Mg I	0.34 ± 0.07	0.29 ± 0.02	0.34 ± 0.03
Si I	0.41 ± 0.08	0.21 ± 0.02	0.31 ± 0.01
Ca I	0.29 ± 0.07	0.33 ± 0.03	0.26 ± 0.01
Sc II	0.15 ± 0.08	0.05 ± 0.03	−0.01 ± 0.02
Ti II	0.19 ± 0.06	0.16 ± 0.02	0.22 ± 0.02
V II	−0.15 ± 0.09	−0.14 ± 0.04	−0.1 ± 0.02
Cr II	−0.07 ± 0.08	−0.13 ± 0.05	
Mn I	−0.39 ± 0.06	−0.39 ± 0.03	−0.25 ± 0.02
Co I	0.00 ± 0.09	−0.06 ± 0.03	
Ni I	−0.08 ± 0.05	−0.12 ± 0.02	−0.05 ± 0.01
Cu I	−0.92 ± 0.06	−0.53 ± 0.02	
Zn I	0.16 ± 0.11	+0.43	
Zr I	0.10 ± 0.11	−0.10 ± 0.12	
Ba II	0.09 ± 0.10	−0.08 ± 0.04	0.16 ± 0.02
La II	−0.02 ± 0.11	+0.18 ± 0.07	0.02 ± 0.02
Eu II	0.44 ± 0.09	+0.56 ± 0.02	0.43 ± 0.02
Al	0.20 ± 0.25	0.44 ± 0.05	
C	−0.27 ± 0.25		
N	0.63 ± 0.45		
Ti II	0.29 ± 0.07		
V II	0.03 ± 0.11		
Cr II	0.02 ± 0.08		
Sr	−0.40 ± 0.05		
Y II	−0.20 ± 0.10		
Zr II	0.29 ± 0.12		
Mo	−0.10 ± 0.08		
Ce II	−0.10 ± 0.12		
Pr II	0.21 ± 0.19		
Nd II	0.05 ± 0.09		
Sm II	0.23 ± 0.10		
Dy II	0.36 ± 0.17		
Th II	0.29 ± 0.05		

along with a comparison of the reported values. Chapter 4 details the error calculations and uncertainties involved with the model atmospheres used. Chapter 5 discusses the results presented in the previous chapters. Chapter 6 summarises the conclusions of this work.

2

Analysis Method

2.1 Observation Data

The stars selected for this study were situated near the RGB tip in the CMD of M5. The spectroscopic data for the 55 stars used in this project were obtained with the Hectochelle instrument, a single-order multi-object spectrograph on the Multiple Mirror Telescope (MMT). The MMT is located on the summit of Mount Hopkins (~ 2606m. above sea level) in Arizona, USA and has a classical Cassegrain design with a primary diameter of 6.5m. The observations were taken on the nights of 17^{th} May 2014 and 15^{th} June 2014 using the OB26, CJ26, RV31 settings (central wavelengths 6632, 6260, 5230 Å, respectively). The weather conditions were clear with $\sim 1''$ of seeing. The filters were setup to have a slow readout in a 2×1 (spatial × dispersion) binning mode. The data were reduced by the SAO telescope data centre's Hectochelle pipeline. The signal-to-noise ratio (SNR) of the OB26 spectra varied from 74 to 13. The majority of the useful lines were present in the CJ26 and RV31 settings.

2.2 Equivalent Width Measurement

The equivalent width (EW) measures the strength of the absorption line in a spectra. It is defined as the width of a rectangle whose area is equal to that of the line profile with

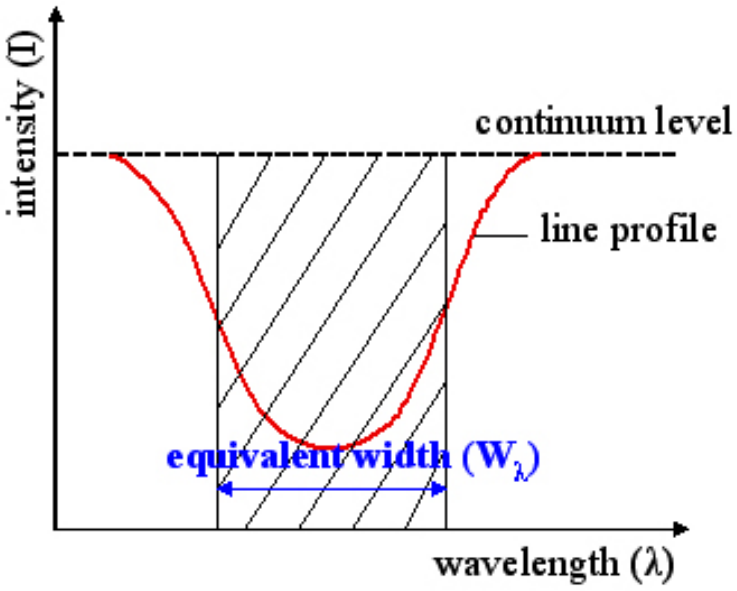

Figure 2.1: Pictorial definition of equivalent width. Image Credit:`www.wikipedia.org`

respect to the continuum, with the height set to the continuum level (see Figure 2.1). Equivalent width is usually expressed in terms of the wavelength unit of the spectrum, in this case angstroms (Å). Mathematically, it is defined as:

$$W_\lambda = \int (1 - \frac{F_\lambda}{F_o}) d\lambda \tag{2.1}$$

where W_λ is the EW, F_o represents the continuum level and F_λ represents the intensity at wavelength λ. Therefore, in order to make accurate EW measurements, we need to know the continuum level and the line profile.

The EWs were measured using software provided by Christian Johnson. The program, written in PYTHON and FORTRAN, uses the stellar spectrum and an input linelist to select particular absoption lines and measure their EWs by fitting Gaussian profiles to them. The measurement procedure is described as follows:

- First, the star's Doppler shift is removed by comparing the star spectrum with a guide spectrum. The high resolution spectrum of Arcturus by Hinkle et al. (2000)

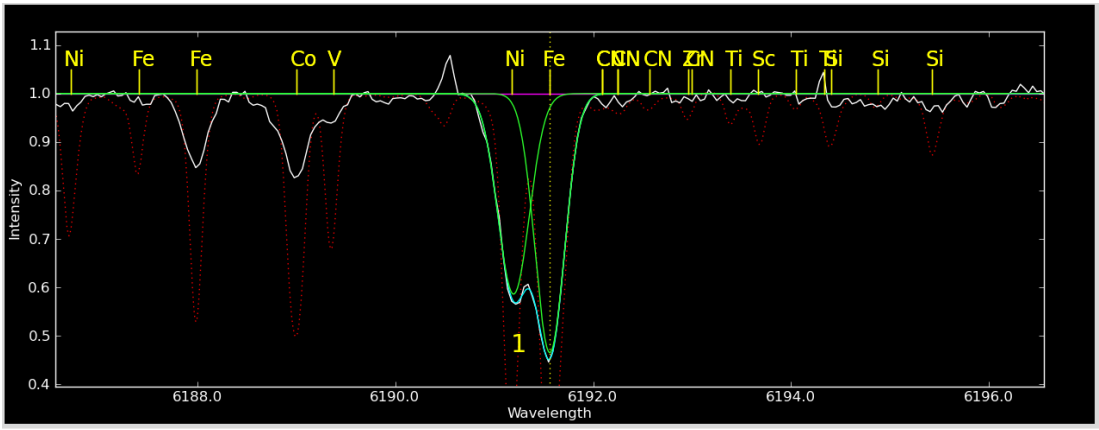

Figure 2.2: The figure shows the EW measurement software interface. The stellar spectrum is shown in white while the reference spectrum is shown in red. The local continuum level is shown by the magenta line. Also shown here is an example of deblending. The iron and nickel lines are close to each other and need to be deblended to get the correct EW. The individual gaussian fits are shown in green and the combined fit is shown in cyan

is used as the guide and a wavelength shift is performed on the star spectrum to match the spectral lines.

- Second, the continuum level of the spectrum has to be set. This is probably the most difficult and important step in measuring the EWs since the value of EW for weak lines is greatly affected by the continuum level (as inferred from equation 2.1). After much discussions and trials, it was agreed upon to set the continuum level locally by distributing the noise points evenly above and below the continuum level.

- Once the continuum is set the program can be used to fit a Gaussian profile individually for the spectral line from the linelist. In cases where the lines were blended, upto five Gaussians can be fit to de-blend lines and obtain the EW for the targeted line (see Figure 2.2).

As a first step, only the Fe I and Fe II line EWs are measured. Table 2.1 shows the linelist used. Care has to be taken to choose lines which have reliable oscillator strength values. For this reason we have chosen a linelist compiled from Johnson et

al. (2012–2015) where these values have been checked against the solar and Arcturus spectra. The program automatically saves the measured EWs in a format which can be readily used by the MOOG software (discussed in the next subsection).

Table 2.1: The full linelist used in this study. The first column gives the line wavelength in Å, the second column gives the ion species, the third column gives the excitation potential (E.P.) for the transition in electron Volts ,and the fourth column gives the weighted oscillator strength for the selected line transition.

Wavelength (Å)	Ion Species	E.P. (eV)	$\log(gf)$ (dex)	Grating
6142.49	Si I	5.62	−1.48	CJ26
6145.02	Si I	5.61	−1.4	CJ26
6155.15	Si I	5.62	−0.75	CJ26
5261.7	Ca I	2.52	−0.59	RV31
6161.29	Ca I	2.52	−1.29	CJ26
6162.17	Ca I	1.9	−0.09	CJ26
6166.44	Ca I	2.52	−1.16	CJ26
6169.04	Ca I	2.52	−0.8	CJ26
6169.56	Ca I	2.53	−0.53	CJ26
5145.46	Ti I	1.46	−0.57	RV31
5147.47	Ti I	0	−2.01	RV31
5210.38	Ti I	0.05	−0.88	RV31
5219.7	Ti I	0.02	−2.29	RV31
6258.1	Ti I	1.44	−0.36	CJ26
6258.7	Ti I	1.46	−0.24	CJ26
6261.1	Ti I	1.43	−0.48	CJ26
5185.91	Ti II	1.89	−1.35	RV31
5225.81	Cr I	2.71	−1.5	RV31
5247.57	Cr I	0.96	−1.59	RV31

Table 2.1 – *Continued from previous page*

Wavelength (Å)	Ion Species	E.P. (eV)	log(gf) (dex)	Grating
5137.38	Fe I	4.178	−0.4	RV31
5141.74	Fe I	2.424	−1.964	RV31
5145.09	Fe I	2.198	−3.266	RV31
5159.06	Fe I	4.283	−0.82	RV31
5162.27	Fe I	4.178	0.09	RV31
5191.45	Fe I	3.038	−0.551	RV31
5194.94	Fe I	1.557	−2.15	RV31
5195.47	Fe I	4.22	−0.086	RV31
5197.94	Fe I	4.301	−1.58	RV31
5198.71	Fe I	2.223	−2.135	RV31
5215.18	Fe I	3.266	−0.801	RV31
5216.27	Fe I	1.608	−2.15	RV31
5217.39	Fe I	3.21	−1.07	RV31
5217.92	Fe I	3.64	−2.139	RV31
5218.51	Fe I	4.58	−2.62	RV31
5226.86	Fe I	3.038	−0.555	RV31
5227.19	Fe I	1.557	−1.228	RV31
5228.38	Fe I	4.22	−1.16	RV31
5232.94	Fe I	2.94	−0.028	RV31
5236.2	Fe I	4.186	−1.737	RV31
5238.25	Fe I	3.98	−3.15	RV31
5242.49	Fe I	3.634	−0.967	RV31
5243.78	Fe I	4.256	−1.11	RV31
5253.46	Fe I	3.283	−1.573	RV31
5254.95	Fe I	0.11	−4.764	RV31

Table 2.1 – *Continued from previous page*

Wavelength (Å)	Ion Species	E.P. (eV)	log(gf) (dex)	Grating
5266.56	Fe I	2.998	−0.386	RV31
5273.16	Fe I	3.292	−0.993	RV31
5273.37	Fe I	2.484	−2.158	RV31
5281.79	Fe I	3.038	−0.834	RV31
5285.13	Fe I	4.43	−1.64	RV31
5295.31	Fe I	4.415	−1.69	RV31
5307.36	Fe I	1.608	−2.987	RV31
5317.52	Fe I	4.14	−2.462	RV31
5318.03	Fe I	3.018	−4.078	RV31
6136.61	Fe I	2.453	−1.4	CJ26
6136.99	Fe I	2.198	−2.95	CJ26
6151.62	Fe I	2.176	−3.31	CJ26
6157.73	Fe I	4.076	−1.19	CJ26
6159.37	Fe I	4.607	−1.88	CJ26
6165.36	Fe I	4.143	−1.54	CJ26
6173.33	Fe I	2.223	−2.89	CJ26
6180.2	Fe I	2.727	−2.71	CJ26
6187.4	Fe I	2.83	−4.14	CJ26
6187.99	Fe I	3.943	−1.75	CJ26
6188.99	Fe I	5.446	−5.572	CJ26
6191.56	Fe I	2.433	−1.417	CJ26
6200.31	Fe I	2.61	−2.33	CJ26
6213.43	Fe I	2.223	−2.52	CJ26
6219.28	Fe I	2.198	−2.33	CJ26
6230.72	Fe I	2.559	−1.281	CJ26

Table 2.1 – *Continued from previous page*

Wavelength (Å)	Ion Species	E.P. (eV)	log(gf) (dex)	Grating
6232.64	Fe I	3.654	−1.24	CJ26
6240.65	Fe I	2.223	−3.32	CJ26
6246.32	Fe I	3.6	−0.77	CJ26
6252.56	Fe I	2.404	−1.63	CJ26
6265.13	Fe I	2.176	−2.55	CJ26
6270.22	Fe I	2.858	−2.62	CJ26
6297.79	Fe I	2.22	−2.67	CJ26
6301.5	Fe I	3.65	−0.67	CJ26
6302.49	Fe I	3.69	−1.12	CJ26
6307.85	Fe I	3.64	−3.27	CJ26
6311.5	Fe I	2.83	−3.17	CJ26
6318.02	Fe I	2.453	−2.261	CJ26
6546.24	Fe I	2.758	−1.71	OB26
6551.68	Fe I	0.99	−5.73	OB26
6556.79	Fe I	4.796	−1.61	OB26
6569.21	Fe I	4.733	−0.21	OB26
6574.23	Fe I	0.99	−5.023	OB26
6575.02	Fe I	2.588	−2.71	OB26
6581.21	Fe I	1.485	−4.73	OB26
6592.91	Fe I	2.727	−1.51	OB26
6593.87	Fe I	2.433	−2.25	OB26
6597.56	Fe I	4.795	−0.98	OB26
6609.11	Fe I	2.559	−2.58	OB26
6646.93	Fe I	2.608	−3.99	OB26
6667.17	Fe I	2.424	−4.956	OB26

Table 2.1 – *Continued from previous page*

Wavelength (Å)	Ion Species	E.P. (eV)	log(gf) (dex)	Grating
6667.42	Fe I	2.45	−4.43	OB26
6677.98	Fe I	2.692	−1.418	OB26
6692.27	Fe I	4.08	−3.15	OB26
6699.14	Fe I	4.59	−2.101	OB26
6703.57	Fe I	2.758	−3.16	OB26
6704.48	Fe I	4.22	−2.6	OB26
6705.1	Fe I	4.607	−1.392	OB26
5197.58	Fe II	3.23	−2.054	RV31
5234.63	Fe II	3.221	−2.219	RV31
6149.26	Fe II	3.889	−2.66	CJ26
6238.39	Fe II	3.889	−2.754	CJ26
6247.56	Fe II	3.892	−2.33	CJ26
6627.26	Fe II	7.27	−1.768	OB26
5200.41	Y II	0.99	−0.57	RV31
5205.73	Y II	1.03	−0.34	RV31
5289.82	Y II	1.03	−1.85	RV31
5274.23	Ce II	1.04	0.13	RV31
5212.36	Nd II	0.2	−0.96	RV31
5249.58	Nd II	0.98	0.2	RV31
6170.06	Er II	0.06	−2.77	CJ26

2.3 Stellar Parameters

Traditionally Fe I and Fe II EWs are used to determine the stellar parameters: Effective temperature (T_{eff}), Surface gravity (log(g)), and Micro-turbulent velocity (v_t). The

abfind driver from the 2010 versioin of MOOG (Sneden et al. 2012) is used to derive the elemental abundance in log(ϵ) notation, ϵ is the number of atoms of that element relative to 10^{12} atoms of hydrogen. It can be converted to [X/H] notation by subtracting the solar value. The MOOG software requires a model atmosphere and the EW tables as input. The output is the average element abundance along with plots of abundance with E.P., reduced EW, and wavelength.

2.3.1 Model Atmospheres

The model atmospheres used in MOOG were created by the α-enhanced ATLAS9 grid (Castelli and Kurucz 2004). These LTE models generally break the stellar photosphere into multiple layers with each layer satisfying both the hydrostatic (pressure–gravity) equilibrium and radiation transfer equations assuming a blackbody source function. In order to get the iron abundance, we first create a model atmosphere with our initial guesses for the stellar parameters.

2.3.2 Abundance dependance with stellar parameters

Equations 2.2 and 2.3 show how Fe I and Fe II abundances are related to T_{eff} and log(g). These can be derived from the basic Saha–Boltzmann equation as shown in Takeda et al. (2002):

$$\epsilon_{FeI} \propto T_{eff}^{3/2} e^{-(\chi_{ion}-\chi_i)/(kT_{eff})} \tag{2.2}$$

$$\epsilon_{FeII} \propto e^{\chi_i/(kT_{eff})} g^{1/3} \tag{2.3}$$

where χ_{ion} is the iron first ionization potential of 7.9 eV, χ_i is the E.P. of i_{th} level and k is the Boltzmann constant. As inferred from the above equations, Fe I abundance is affected by T_{eff} and almost independent (indirectly dependent through excitation potential) of log(g) while Fe II line abundance is greatly affected by log(g). Thus we use three conditions to constrain the three parameters.

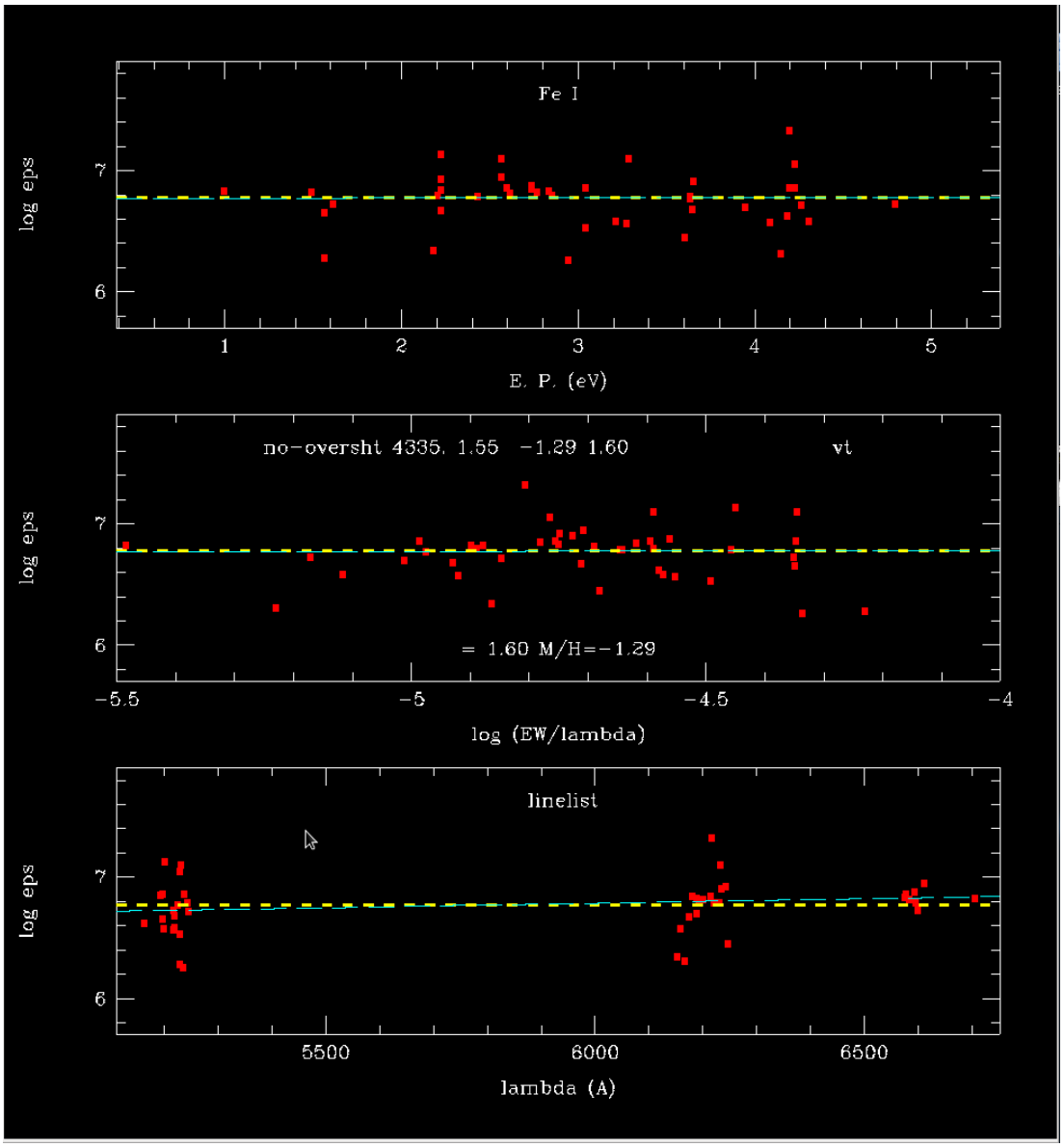

Figure 2.3: This output window of MOOG show three plots: the top plot is log(ϵ) against E.P., the middle plot is log(ϵ) against reduced EW, and the bottom one is log(ϵ) against wavelength. The cyan line shows the trend while the yellow line shows the mean value.

Excitation Equilibrium : Due to the sensitivity of T_{eff} on ϵ_{FeI}, we constrain it by requiring the FeI abundance to be independent of E.P. over a sufficient range.

Variation with reduced EW : The microturbulence velocity, v_t, is defined as non-thermal component of the gas velocity within the region of spectral line formation (Cantiello et al. 2009). A plot of the equivalent width as a function of the number of absorbing atoms is called the curve of growth. The microturbulence velocity was introduced into the Doppler width of the line opacity function to account for the difference in the calculated and observed line strengths of saturated lines near the flat part of the curve of growth (Takeda et al. 2002). This parameter thus only affects strong lines and can be constrained by making the abundance independent of reduced EWs. Since fewer Fe II lines are measured only Fe I abundance was made to satisfy this condition.

Ionization Equilibrium : Fe II is greatly affected by log(g) while Fe I is almost independent of it. Thus we impose a condition that the average abundance derived from both Fe I and Fe II to be approximately equal to constrain log(g).

There may be some outlier points in the MOOG plots which are removed after fixing the T_{eff} and v_t using Fe I lines. The Fe I abundance points which have a difference more than three times the standard deviation are removed and the Fe I abundance is refined before proceeding to match Fe II abundance.

Due to the interdependence of the three parameters we employ an iterative procedure to converge upon the optimal parameters. Once the stellar parameters are found, we proceed onto the measurement of other elements. Figure 2.4 shows the schematic of the method followed.

2.3.3 Stellar Parameters

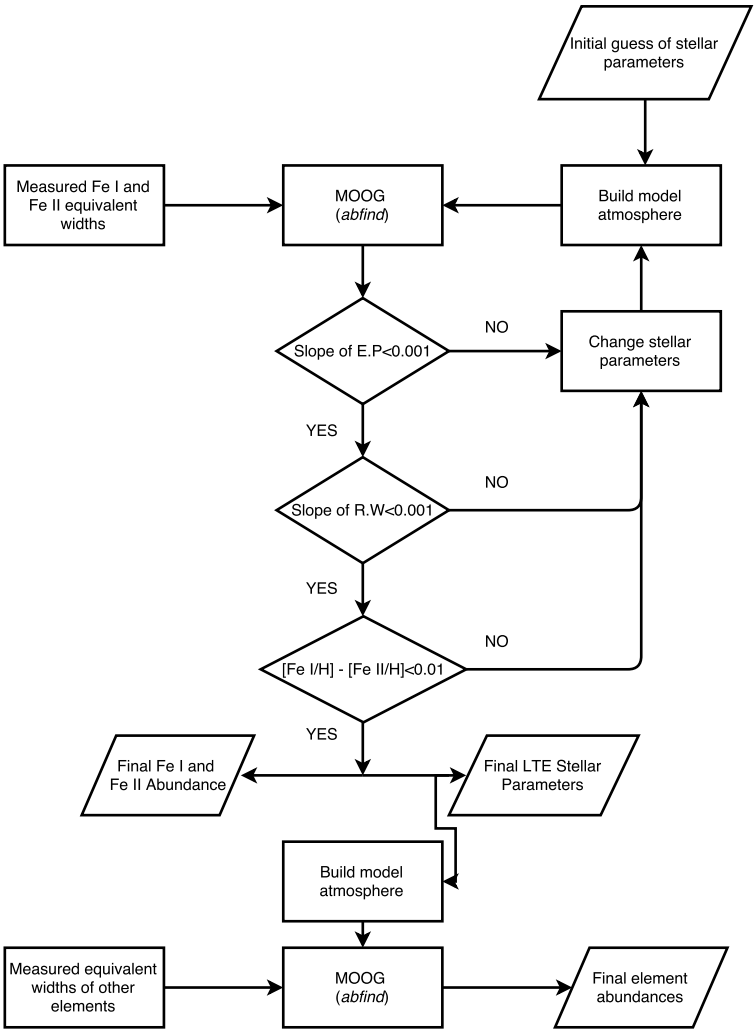

Figure 2.4: A schematic representation of the analysis procedure followed.

Table 2.2: The stellar parameter results are tabulated. The 2MASS identifiers of the stars are used where possible. The errors associated with the measurements are discussed in Chapter 4.

Star ID	RA (J2000)	Dec (J2000)	T_{eff} (K)	log(g) (dex)	[Fe/H] (dex)	v_t (kms^{-1})
15184164+0203533	15:18:41.65	02:03:53.3	4180	0.6	−1.3	1.86
15183505+0201068	15:18:35.05	02:01:6.9	4210	0.91	−1.17	1.68
15182262+0200305	15:18:22.62	02:00:30.6	4245	0.355	−1.19	1.88
15183583+0203421	15:18:35.83	02:03:42.1	4286	1.38	−1.182	2.52
15182938+0208275	15:18:29.39	02:08:27.6	4314	1.275	−1.21	2.17
15182717+0159524	15:18:27.18	01:59:52.4	4332	1.24	−1.16	1.67
15183223+0201341	15:18:32.23	02:01:34.1	4341	1.52	−1.015	1.68
15182324+0159163	15:18:23.25	01:59:16.3	4353	1.08	−1.26	1.68
15180537+0202015	15:18:5.38	02:02:1.5	4387	1.25	−1.13	1.79
15180892+0206285	15:18:8.93	02:06:28.5	4392	0.84	−1.31	1.83
15182345+0159572	15:18:23.46	01:59:57.2	4396	0.9	−1.31	2
15184449+0202053	15:18:44.5	02:02:5.3	4413	1.29	−1.3	1.7
15184001+0211023	15:18:40.01	02:11:2.4	4433	1.14	−1.265	1.67
15182594+0203108	15:18:25.95	02:03:10.9	4484	1.56	−1.15	1.74
15184120+0201511	15:18:41.2	02:01:51.1	4515	1.73	−1.09	1.65
15183693+0204389	15:18:36.93	02:04:39	4525	0.96	−1.375	1.58
15184052+0207337	15:18:40.52	02:07:33.7	4577	1.55	−1.11	1.58
15180407+0205557	15:18:4.08	02:05:55.8	4580	1.94	−1.07	1.64
15190237+0204586	15:19:2.38	02:04:58.6	4619	1.62	−1.47	1.77
6	15:19:2.45	02:13:50.2	4626	1.4	−1.37	1.73
15183463+0209313	15:18:34.63	02:09:31.3	4640	1.32	−1.17	1.7
15183815+0203219	15:18:38.15	02:03:22	4642	1.04	−1.395	1.55
15182624+0205545	15:18:26.25	02:05:54.6	4645	1.87	−1.155	1.74

Table 2.2 – *Continued from previous page*

Star ID	RA (J2000)	Dec (J2000)	T_{eff} (K)	log(g) (dex)	[Fe/H] (dex)	v_t (kms^{-1})
15183481+0202226	15:18:34.81	02:02:22.6	4651	1.23	−1.395	1.7
15185420+0205473	15:18:54.2	02:05:47.3	4660	1.53	−1.32	1.53
1	15:18:34.43	02:27:45	4667	2.17	−1.205	1.44
15184114+0205528	15:18:41.14	02:05:52.8	4674	1.89	−1.075	1.3
15182581+0204552	15:18:25.82	02:04:55.3	4675	1.21	−1.32	1.59
15183182+0203277	15:18:31.82	02:03:27.8	4690	1.71	−1.34	1.63
15184730+0207253	15:18:47.31	02:07:25.4	4699	0.375	−1.83	2.16
15181172+0202519	15:18:11.73	02:02:52	4706	1.27	−1.39	1.95
15183086+0212167	15:18:30.86	02:12:16.7	4710	1.92	−1.165	1.51
15183638+0208507	15:18:36.39	02:08:50.8	4728	0.71	−1.38	1.76
15183050+0209224	15:18:30.5	02:09:22.4	4734	2.028	−1.19	1.44
15184864+0205290	15:18:48.64	02:05:29.1	4750	1.07	−1.46	1.91
15184833+0206520	15:18:48.36	02:06:52	4769	1.65	−1.36	1.42
15184734+0202509	15:18:47.34	02:02:50.9	4770	1.1	−1.61	1.84
15185731+0203077	15:18:57.31	02:03:7.7	4781	1.1	−1.52	1.62
15182575+0201461	15:18:25.76	02:01:46.1	4792	1.57	−1.25	1.97
15183978+0201101	15:18:39.78	02:01:10.2	4810	1.43	−1.255	1.67
15182072+0206414	15:18:20.72	02:06:41.4	4819	2.32	−0.98	1.46
15181418+0201222	15:18:14.18	02:01:22.2	4874	0.9	−1.65	1.89
15181803+0203503	15:18:18.04	02:03:50.3	4876	0.95	−1.555	1.98
15183326+0207248	15:18:33.27	02:07:24.8	4897	1.12	−1.46	1.72
15181644+0207177	15:18:16.44	02:07:17.7	4900	1.81	−1.205	1.81
15181126+0206347	15:18:11.26	02:06:34.7	4902	2.14	−1.21	1.66
15183280+0204362	15:18:32.79	02:04:36.4	4919	2.62	−1.03	1.35
15182634+0206502	15:18:26.34	02:06:50.2	4930	1.17	−1.685	1.78

Table 2.2 – *Continued from previous page*

Star ID	RA (J2000)	Dec (J2000)	T_{eff} (K)	log(g) (dex)	[Fe/H] (dex)	v_t (kms^{-1})
15182245+0202242	15:18:22.45	02:02:24.2	4963	2.75	−1	1.61
15182347+0203489	15:18:23.47	02:03:49	4975	1.2	−1.3	1.53
15184233+0207406	15:18:42.33	02:07:40.7	4975	1.24	−1.565	2.28
36	15:19:28.77	02:06:51.1	4871	2.04	−1.22	1.62
15184866+0209472	15:18:48.67	02:09:47.2	5124	1.69	−1.355	1.77
15182264+0210037	15:18:22.65	02:10:3.8	5277	1.52	−1.6	2.16
15181445+0203131	15:18:14.47	02:03:13.2	5320	2.7	−1.025	1.97

3

Results

The average iron abundance is found to be [Fe/H]= -1.29 ± 0.15 dex. The average [Fe /H] value for the cluster from this study is in agreement with Harris (2010) catalogue value of -1.29 dex. From Table 3.1 we can see that our value is consistent with literature. The differences might be related to different solar values used by the authors however the difference should not exceed 0.5 dex. The relative abundance in this study is calculated using the solar values reported by Asplund et al. (2009). The uncertainties related with the measurements are discussed in the next chapter. The abundance measurements for other elements are summarised in Table: 3.10 (at the end of this chapter).

Table 3.1: Comparison between average [Fe/H] values

Study	[Fe/H]
Ivans et al. (2001)	-1.34 ± 0.01
Ramírez and Cohen (2003)	-1.30 ± 0.02
Lai et al. (2011)	-1.51 ± 0.14
This work	-1.29 ± 0.15

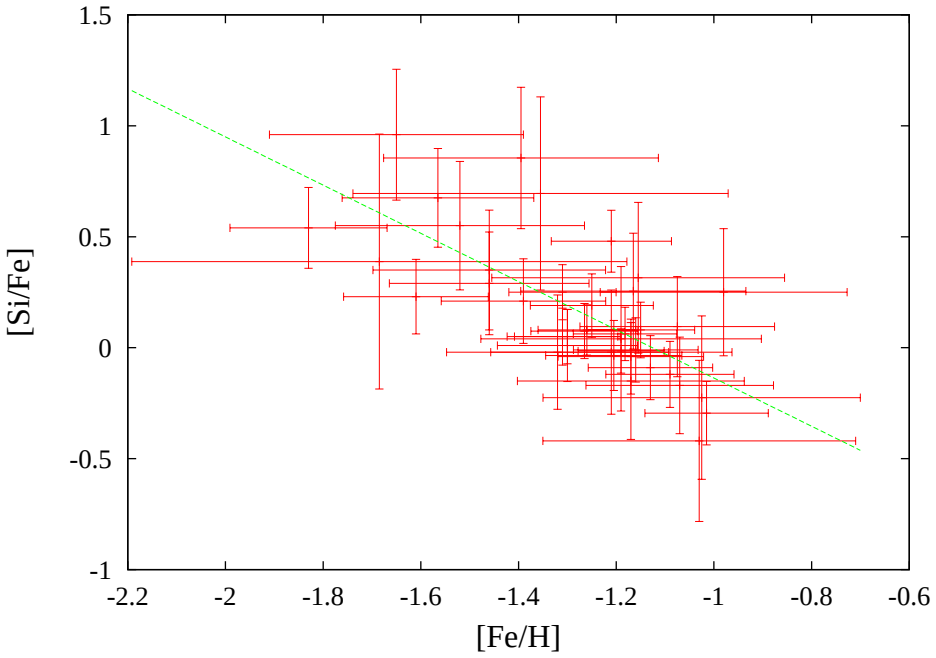

Figure 3.1: Plot of [Si/Fe] versus [Fe/H] with a linear fit.

3.1 Silicon

The [Si/Fe] abundance were meaured for only for 39 stars in this study using four Si I lines. The silicon abundance varies from [Si/Fe]= −0.42 to 0.96. The average value is determined to be [Si/Fe]= 0.16 ± 0.17 dex. This is 0.15 dex lower than the cluster average reported by Ivans et al. (2001), 0.05 dex lower than Ramírez and Cohen (2003) and 0.25 dex lower than Lai et al. (2011). This difference can be attributed to the larger number of Si I lines used by the other studies. Figure 3.1 shows the relation between silicon and iron abundance. We find an anti-correlation between them with a slope of −1.087 with an asymptotic error of ±0.179. Although linear fit might look real due to the low asymptotic error, this trend is affected by the spread in the iron abundance and can be considered as artificial.

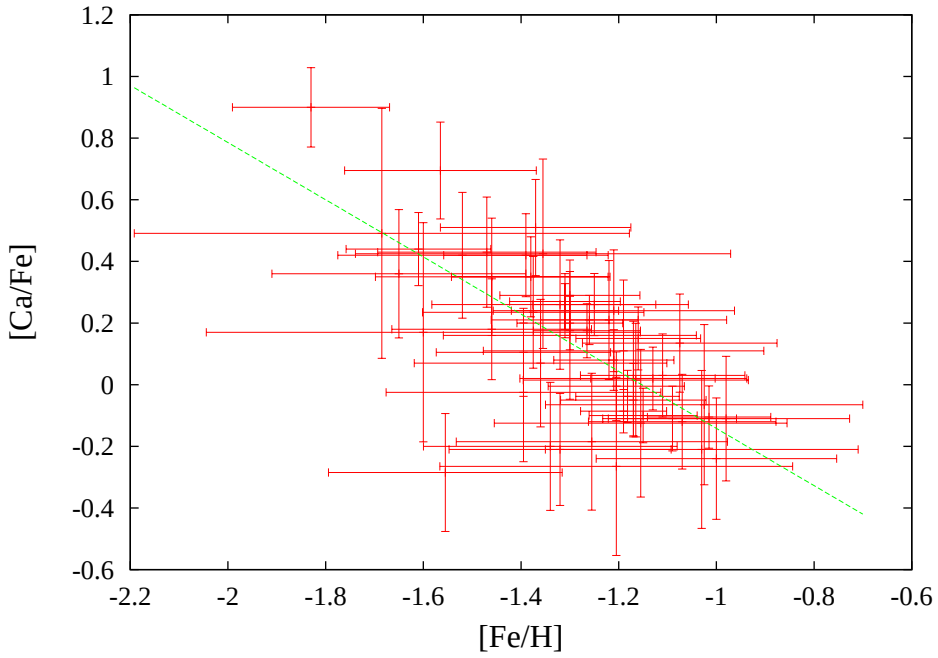

Figure 3.2: Plot of [Ca/Fe] versus [Fe/H] with a linear fit.

3.2 Calcium

The [Ca/Fe] abundances were measured for all the stars in this study using six Ca I lines. The cluster average is [Ca/Fe]= 0.13 ± 0.12 dex. It is 0.13 dex lower than Ivans et al. (2001), 0.2 dex lower than Ramírez and Cohen (2003) and 0.16 dex lower than Lai et al. (2011). We also report a bigger error margin than other studies. Figure 3.2 shows the trend of calcium abundance. Like the silicon abundance, we find a gradient with iron abundance with a slope of -0.928 ± 0.134. This trend is quite noticeable here but it is not seen in any of the other studies. The slope is considered to be due to the iron abundance spread.

3.3 Titanium

The neutral [Ti I/Fe] abundance is measured for all the stars in this study using seven Ti I lines. The average value is 0.4 (to match 0.15) dex. This is 0.18 dex higher than Ivans et al. (2001), 0.24 dex higher than Ramírez and Cohen (2003) and 0.21 dex higher than

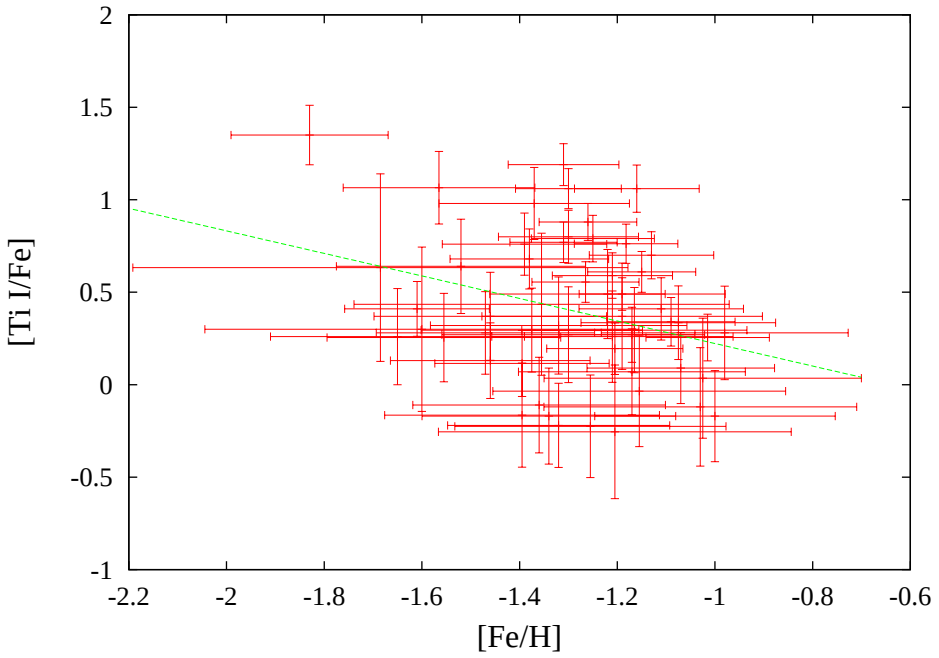

Figure 3.3: Plot of [Ti I/Fe] versus [Fe/H] with a linear fit.

Lai et al. (2011). This shows a similar behaviour with iron abundance as silicon and calcium but with a lesser gradient of -0.609 ± 0.273 as seen in Figure 3.3. The neutral titanium also shows a larger scatter in abundance than silicon and calcium.

For titanium we were also able to measure the abundance of the ionised species using the 5185.91Å line. We report the cluster average as 0.31 ± 0.13 dex. This is seen to be consistent with Lai et al. (2011) where it is 0.02 dex lower. Although ionization equilibrium condition imposed while determining the stellar parameters should give us the same titanium abundance we see an average difference of 0.13 dex between the neutral and ionised species. Two stars in particular, 15182938+0208275 and 15184164+0203533, have very high differences of 0.99 and 1.32 dex. If they are considered as outliers the average difference comes down to an acceptable 0.08 dex. From Figure 3.4 we see a similar trend, as seen in calcium, having a gradient of -0.943 ± 0.273.

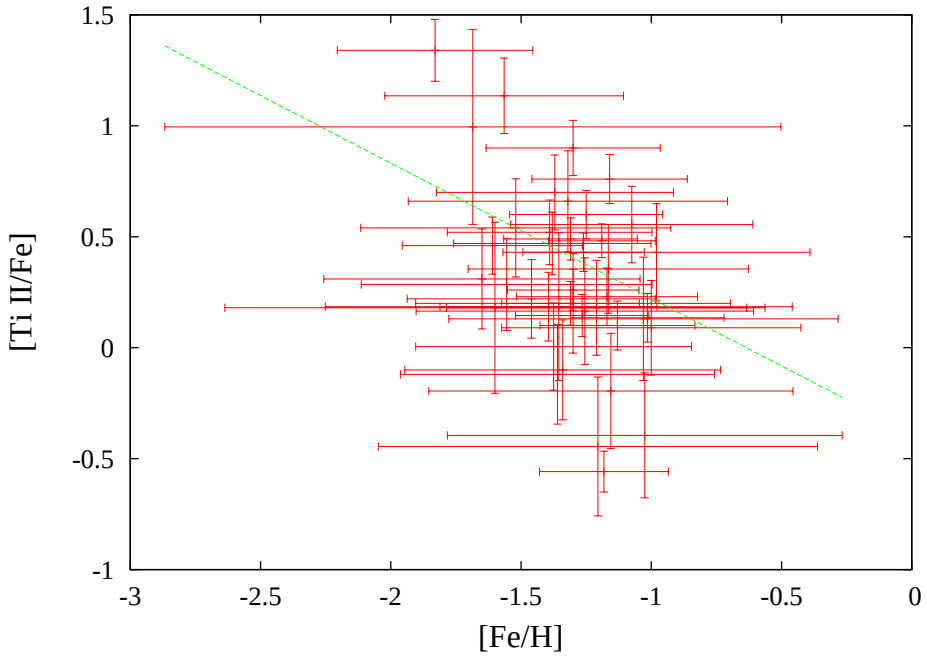

Figure 3.4: Plot of [Ti II/Fe] versus [Fe/H] with a linear fit.

3.4 α Elements

The combined variation of silicon, calcium and titanium should give us a better understanding of the data as it will reduce the scatter in them. The α-element abundance is calculated as $[\alpha/Fe] = \frac{([Si/Fe]+[Ca/Fe]+[Ti/Fe])}{3}$. This is limited to the 39 stars which have all three measurements. Only the neutral ion abundances were used. Figure 3.5 shows that α-elements variation is similar to calcium with a slope of -0.953 ± 0.133. Due to the large scatter seen with iron abundance it is inconclusive whether this trend might be real.

3.5 Chromium

The chromium abundance is found for 42 stars in the sample using the Cr I lines. The average [Cr/Fe] abundance is found to be 0.10 ± 0.41 dex. The main source of error comes from the measurement of the weak 5225.81 Å line. This average value is 0.23 dex higher than Ramírez and Cohen (2003) and 0.17 dex higher than Lai et al. (2011).

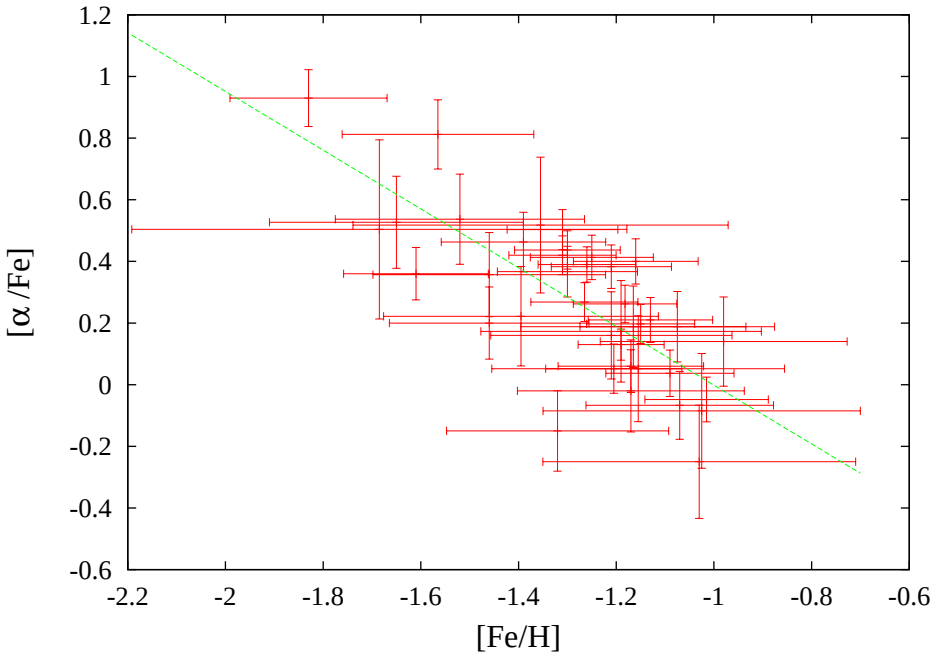

Figure 3.5: Plot of [α/Fe] versus [Fe/H] with a linear fit.

Figure 3.6 shows the relation with iron abundance. The linear fit shows a gradient of -0.669 ± 0.211.

3.6 Yttrium

The yttrium abundance is measured for 42 stars in the sample using the Y II lines. The average is [Y/ Fe]=0.01 ± 0.16 dex. This is 0.21 dex higher than Lai et al. (2011). Figure 3.7 shows the trend with iron abundance. It has a slope of -0.684 ± 0.287 with [Fe/H].

3.7 Cerium

The cerium abundance is measured for 34 stars in the sample using the Ce II 5274.23 Å line. The cluster average is [Ce/Fe]= 0.13 ± 0.13 dex. This is 0.23 dex higher than Lai et al. (2011). Figure 3.8 shows the trend with iron abundance. It has a slope of

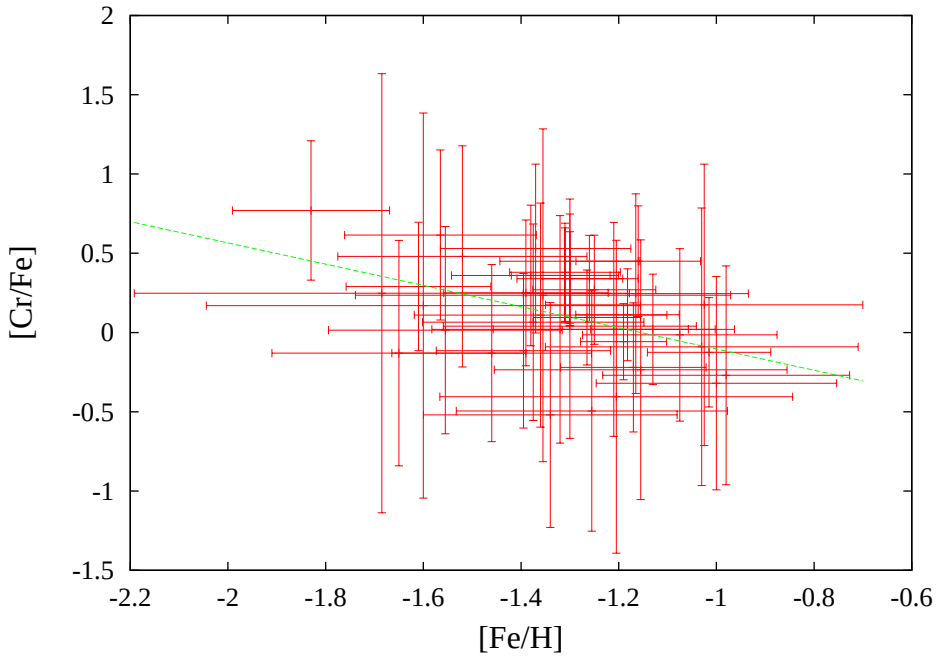

Figure 3.6: Plot of [Cr/Fe] versus [Fe/H] with a linear fit.

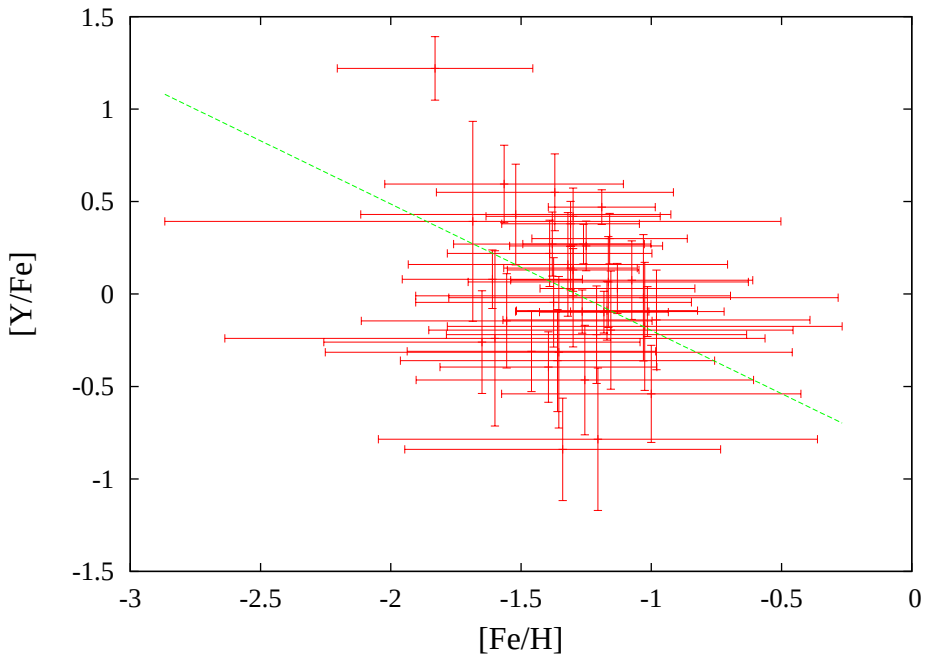

Figure 3.7: Plot of [Y/Fe] versus [Fe/H] with a linear fit.

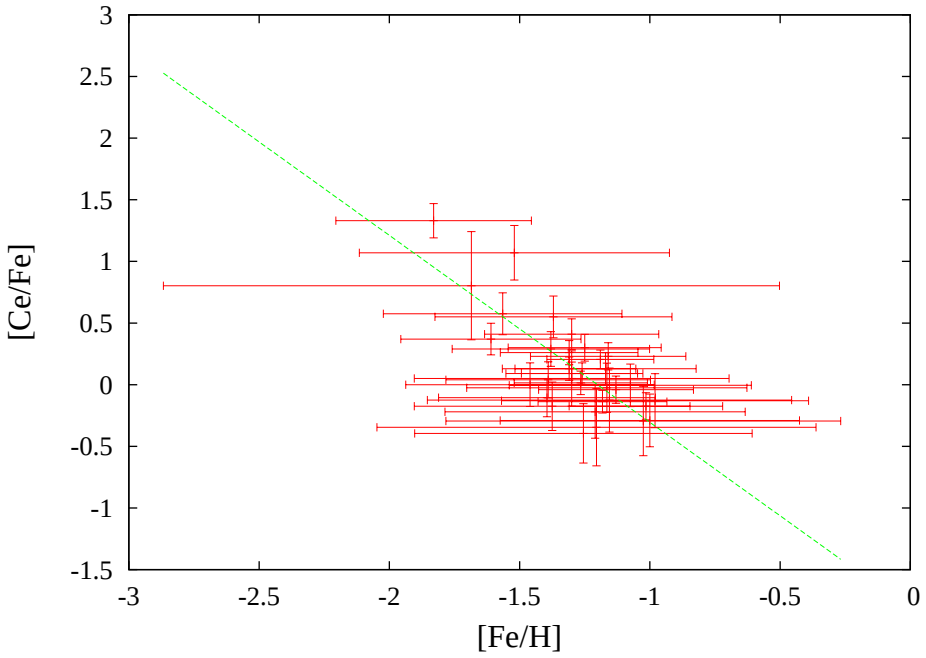

Figure 3.8: Plot of [Ce/Fe] versus [Fe/H] with a linear fit.

-1.516 ± 0.225. The strong anti-correlation arises as an artefact due to the metallicity spread.

3.8 Neodymium

Neodynium abundance is measured for 40 stars in the sample using the Nd II lines. the cluster average is [Nd/Fe]= 0.52±0.14 dex. This is 0.47 dex higer than Lai et al. (2011). Figure 3.9 show its variation with [Fe/H]. The trend has a slope of -0.892 ± 0.302.

3.9 Erbium

Erbium abundance is measured using the Er II 6170 Å line. The cluster average is [Er/Fe]= 1.27 ± 0.18 dex. This shows a strong anti-correlation with iron abundance with a slope of -1.45 ± 0.825 dex. Figure 3.10 shows its variation with iron abundance. There is a huge scatter in the data.

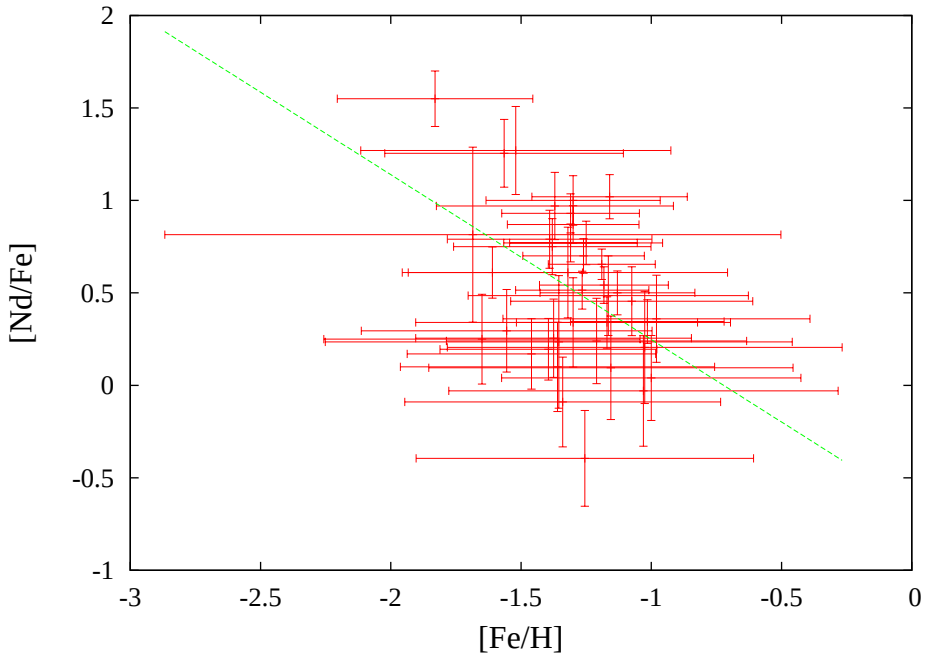

Figure 3.9: Plot of [Nd/Fe] versus [Fe/H] with a linear fit.

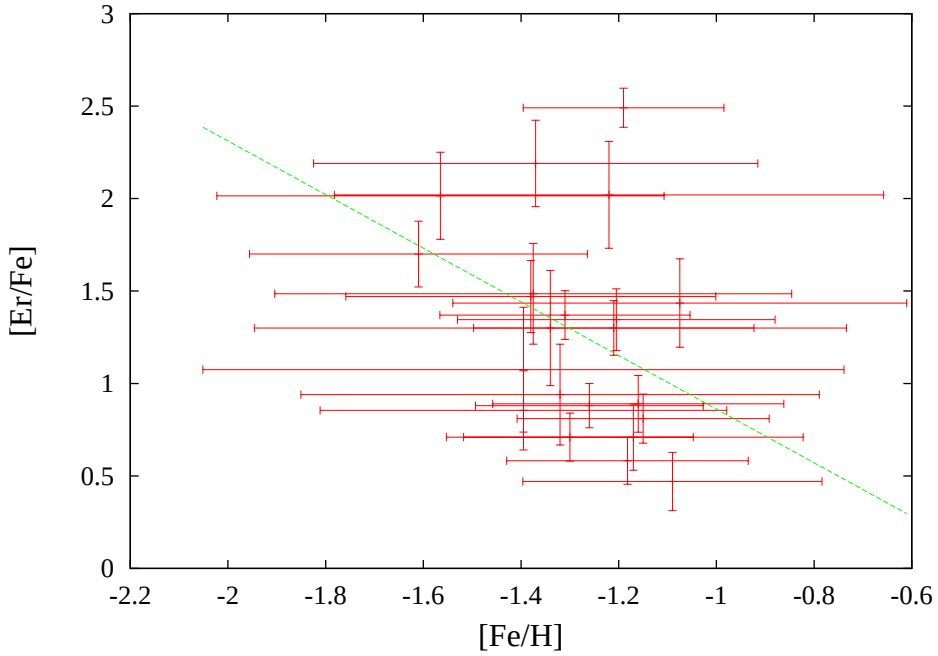

Figure 3.10: Plot of [Er/Fe] versus [Fe/H] with a linear fit.

3.10 Summary

In conclusion all the other element abundances show a consistent anti-correlation with iron abundance but this artificial trend is expected to arise out of the spread in iron abundances. These artificial trends can be diminished by handling errors more rigorously. The mean abundances of [Fe I/H], [Si I/Fe I], [Ca I/Fe I] and [Ti I/Fe I] are considered to be good when compared with the literature values. This study shares 11, 2 and 1 star in common with Ivans et al. (2001), Lai et al. (2011) and Yong et al. (2008), respectively. The differences in the reported and observed stellar parameters are tabulated in Table 3.2.

Table 3.2: The comparison of the stellar parameters in this study with literature values. References: (1)Ivans et al. (2001); (2) Lai et al. (2011); (3) Yong et al. (2008); (4)This work

Star	T_{eff} K	[Fe/H] dex	log(g) dex	v_t km s^{-1}	Δ [Fe/H] dex	Δ T_{eff} K	Δ log(g) dex	Δv_t km s^{-1}
15184164 + 0203533[1]	4110	−1.34	0.5	1.85				
15184164 + 0203533[4]	4180	−1.3	0.6	1.86	−0.04	−70	−0.1	−0.01
15182262 + 0200305[2]	4100	−1.3	0.66	1.81				
15182262 + 0200305[4]	4245	−1.19	1.015	1.88	−0.11	−145	−0.355	−0.07
15182345 + 0159572[1]	4257	−1.29	0.96	1.55				
15182345 + 0159572[4]	4396	−1.31	0.9	2	0.02	−139	0.06	−0.45
15182938 + 0208275[1]	4050	−1.34	0.45	1.85				
15182938 + 0208275[4]	4314	−1.21	1.275	2.17	−0.13	−264	−0.825	−0.32
15184120 + 0201511[1]	4275	−1.28	0.65	1.55				
15184120 + 0201511[4]	4515	−1.09	1.73	1.65	−0.19	−240	−1.08	−0.1
15183505 + 0201068[1]	4125	−1.39	0.5	1.7				
15183505 + 0201068[4]	4210	−1.17	0.91	1.68	−0.22	−85	−0.41	0.02
15183223 + 0201341[1]	4154	−1.32	0.78	1.95				
15183223 + 0201341[4]	4341	−1.015	1.52	1.68	−0.305	−187	−0.74	0.27
15184449 + 0202053[3]	4400	−1.33	1.2	1.75				
15184449 + 0202053[4]	4413	−1.3	1.29	1.7	−0.03	−13	−0.09	0.05
15184052 + 0207337[1]	4400	−1.32	1	1.5				
15184052 + 0207337[4]	4577	−1.11	1.55	1.58	−0.21	−123	0.29	−0.08
15183638 + 0208507[1]	4700	−1.47	0.85	1.8				
15183638 + 0208507[4]	4728	−1.39	0.71	1.76	−0.08	−28	0.04	0.04
15182072 + 0206414[1]	4525	−1.24	1.15	1.35				
15182072 + 0206414[4]	4819	−0.98	2.32	1.46	−0.26	−294	−0.11	−0.11
15183481 + 0202226[1]	4625	−1.24	1.55	1.2				
15183481 + 0202226[4]	4651	−1.395	1.23	1.7	0.155	−26	−0.5	−0.5
15183978 + 0201101[1]	4650	−1.41	1.05	1.4				
15183978 + 0201101[4]	4810	−1.255	1.43	1.67	−0.155	−160	−0.27	−0.27
15184233 + 0207406[2]	4893	−1.66	1.71	1.95				
15184233 + 0207406[4]	4975	−1.565	1.24	2.28	−0.095	−82	−0.33	−0.33

Table 3.3: Measured element abundances

Star ID:	[Fe/H]	[SiI/FeI]	[CaI/FeI]	[TiI/FeI]	[TiII/FeII]	[CrI/FeI]	[YII/FeII]	[CeII/FeII]	[NdII/FeII]	[ErII/FeII]
15184164+0203533	−1.3	0.18	0.08	0.88	−0.44	0.23	0.02	−0.02	0.66	0.7
15183505+0201068	−1.17	−0.05	0.06	0.74	0.14	0.06	0.07	0	0.54	
15182262+0200305	−1.19	−0.06	0.09	0.95	0.15	0.23	0.02	−0.02	0.76	0.6
15183583+0203421	−1.182	−0.023	−0.094	0.482	0.474	−0.066	0.462	0.197	0.647	2.483
15182938+0208275	−1.21	−0.05	0.17	1.09	0.1	0.28	0.28	0.16	0.83	
15182717+0159524	−1.16	0.09	−0.09	0.62						0.82
15183223+0201341	−1.015	−0.155	0.005	0.915	0.615	0.305	0.155	0.085	0.875	0.745
15182324+0159163	−1.26	0.53	0.13	0.64						1.35
15180537+0202015	−1.13	−0.05	0.08	0.75	0.3	0.21	0.14	−0.04	0.57	0.75
15180892+0206285	−1.31	0.1	0.11	0.56						0.69
15182345+0159572	−1.31	0.12	0.22	0.6	0.19	0.14	−0.05	0.06	0.56	
15184449+0202053	−1.3	0.09	0.08	0.4	0.36	−0.09	0.04	0.26	0.47	0.84
15184001+0211023	−1.265	−0.045	0.145	0.505	0.385	0.125	0.155	0.075	0.595	
15182594+0203108	−1.15	0.09	0.08	0.61	0.33	0.2	−0.02	−0.03	0.61	1.21
15184120+0201511	−1.09	0.03	0.1	0.63	0.44	0.11	0.1	0.14	0.61	
15183693+0204389	−1.375	0.135	0.185	0.395						

Table 3.3 – *Continued from previous page*

Star ID:	[Fe/H]	[SiI/FeI]	[CaI/FeI]	[TiI/FeI]	[TiII/FeII]	[CrI/FeI]	[YII/FeII]	[CeII/FeII]	[NdII/FeII]	[ErII/FeII]
15184052+0207337	−1.11	−0.07	0.14	0.48	0.24	−0.03	−0.06	−0.24	0.51	
15180407+0205557	−1.07	−0.22	0.06	0.57	0.67	0.22	0.19	0.18	0.77	
15190237+0204586	−1.47	0.02	0.23	0.32	0.57	0.35	0.42		0.41	
6	−1.37	0.53	0.09	0.18	0.02	−0.02	0.02	0.09	0.31	
15183463+0209313	−1.17		0.09	0.47						
15183815+0203219	−1.395	0.075	0.245	0.295						
15182624+0205545	−1.155		0.125	0.455	0.245	0.135	0.045	0.065	0.525	1.245
15183481+0202226	−1.395		0.255	0.315	0.025	0.085	−0.025	−0.155	0.275	1.505
15185420+0205473	−1.32		0.08	0.15	0.41	0	−0.22	0.03	0.36	
1	−1.205	0.475	0.115	0.505	0.655	−0.045	0.085	0.095	0.585	
15184114+0205528	−1.075	0.095	0.135	0.335	0.555	−0.015	0.075	−0.005	0.455	1.435
15182581+0204552	−1.32	0.21	0.21	0.23						
15183182+0203277	−1.34		0.2	0.31	0.24	0.08	0.03	0.09	0.38	
15184730+0207253	−1.83	1.29	0.41	0.27						1.51
15181172+0202519	−1.39	0.01	0.22	0.19	0.24	0.07	−0.14	0.15	0.39	1.48
15183086+0212167	−1.165	0.255	0.015	0.295	0.355	0.245	0.065	−0.025	0.485	
15183638+0208507	−1.38		0.09	0.1	0.17	−0.13	−0.41	−0.12	0.18	0.84

Table 3.3 – *Continued from previous page*

Star ID:	[Fe/H]	[SiI/FeI]	[CaI/FeI]	[TiI/FeI]	[TiII/FeII]	[CrI/FeI]	[YII/FeII]	[CeII/FeII]	[NdII/FeII]	[ErII/FeII]
15183050+0209224	−1.19		0.13	0.19	0.53	−0.11	0.03		0.48	
15184864+0205290	−1.46	0.29	0.18	0.13	0.22	−0.13	−0.31	0	0.17	
15184833+0206520	−1.36	0.11	0.27	0.37	−0.06	0.51	0.16	0.04	0.54	
15184734+0202509	−1.61	0.27	0.08	0.07						1.23
15185731+0203077	−1.52		0.08	0.04	0.43	−0.23	−0.2	−0.13	−0.13	
15182575+0201461	−1.25	0.01	0.04	0.24						1.39
15183978+0201101	−1.255	0.025	0.285	0.305	0.225	0.065	−0.175	−0.175	0.285	
15182072+0206414	−0.98	0.09	0.11	0.48	0.55	0.03	0.01	−0.01	0.67	1.43
15181418+0201222	−1.65		0.11	0.14	0.21	−0.21	−0.53		0.22	1.61
15181803+0203503	−1.555	0.865	0.265	0.165	0.215	−0.225	−0.355		0.155	
15183326+0207248	−1.46		−0.38	0.16	0.19	−0.08	−0.24		0.2	
15181644+0207177	−1.205	0.055	0.125	0.385						
15181126+0206347	−1.21	0.24	0.11	0.33	0.23	0.17	0.12	0.76	0.96	
15183280+0204362	−1.03	−0.26	0.1	0.55	0.54	−0.03	0.42	0.53	0.75	
15182634+0206502	−1.685		0.215	0.225	0.035	0.075	−0.305	0.135		
15182245+0202242	−1		0.14	0.61	0.33	0.16	0.18	0.18	0.6	1.82
15182347+0203489	−1.3		0.26	0.11						

Table 3.3 – *Continued from previous page*

Star ID:	[Fe/H]	[SiI/FeI]	[CaI/FeI]	[TiI/FeI]	[TiII/FeII]	[CrI/FeI]	[YII/FeII]	[CeII/FeII]	[NdII/FeII]	[ErII/FeII]
15184233+0207406	−1.565		0.275	0.095	0.085	0.315	−0.155		0.305	
36	−1.22	−0.077	0.026	0.168	0.53	−0.217	−0.072	0.338	0.35	
15184866+0209472	−1.355	0.695	0.425	0.435	0.185	0.235	−0.315		0.235	
15182264+0210037	−1.6		0.17	0.3	0.18	0.17	−0.24			
15181445+0203131	−1.025		0.015	0.295						1.825

4

Error Analysis

4.1 Measurement Error

There are two main sources of errors in the abundance measurements. The first source is due to the statistical nature of measurement. The measurement error (σ_{meas}) is characterised by the errors in EW measurement (placement of the continuum, matching of the observed line profile with a Gaussian profile) and the uncertainties in the atomic parameters. It is calculated by:

$$\sigma_{meas} = \frac{\sigma}{\sqrt{N_{lines}}} \tag{4.1}$$

where σ is the standard deviation around the the average abundance value calculated by MOOG and N_{lines} is the number of EW measurements made for that element. The σ_{meas} for the star with the highest and lowest SNR in the OB26 grating is averaged to give the σ_{meas} for the entire sample. Our sample of stars show a SNR variation of 75 to 13 in the OB26 setting with an average SNR of ~44. Therefore to include the effect of SNR, the total error σ_{tot} for each measurement is weighted by a fraction of the average SNR to the stellar SNR. The SNR values seen in the observed sample is tabulated in Table 4.4. From Table 4.1, we can see that the average measurement errors are well within 0.20 dex for all elements with the exception of Cr. The [Cr/Fe] abundance shows increased uncertainty due to the difficulty in the de-blending and weakness of

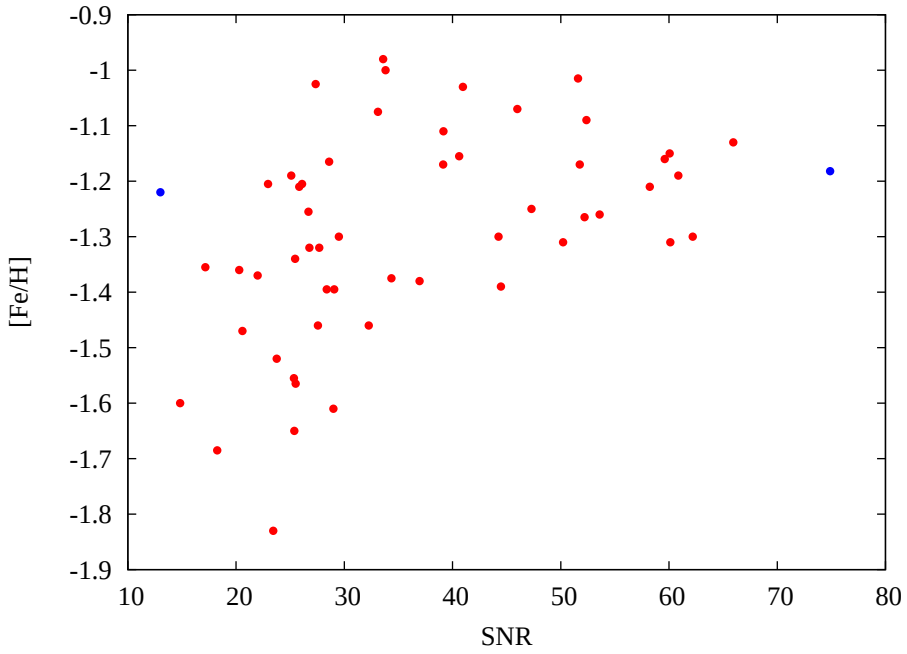

Figure 4.1: Plot showing variation of [Fe/H] with SNR. As expected we see a bigger scatter in [Fe/H] for stars with lower SNR. The two star taken as representative for the sample are shown in blue.

Table 4.1: σ_{meas} for the measured lines

Abundances	Star				Observational Error
	15183583+0203421		36		
	N_{lines}	$\sigma/\sqrt{N_{lines}}$	N_{lines}	$\sigma/\sqrt{N_{lines}}$	σ_{meas}
[Fe I/H]	54	0.03	42	0.03	0.03
[Fe II/H]	5	0.24	4	0.09	0.17
[Si I/Fe I]	1		1		
[Ca I/Fe I]	6	0.09	5	0.1	0.1
[Ti I/Fe I]	5	0.15	5	0.07	0.11
[Ti II/Fe II]	1		1		
[Cr I/Fe I]	2	0.4	1		0.4
[Y II/Fe II]	2	0.18	2	0.04	0.11
[Ce II/Fe II]	1		1		
[Nd II/Fe II]	2	0.04	2	0.06	0.05
[Er II/Fe II]	1				

the 5225.8 Å spectral line.

4.2 Error due to Stellar Parameter Uncertainty

The second source of error is due to the uncertainties in the stellar parameters (or model atmosphere) (σ_{atm}). This is calculated by studying the variation of abundance with each stellar parameter separately. Each stellar parameter is perturbed one at a time while keeping the other parameters same and its effect on the abundance is noted. Here again the stars with the highest and the lowest SNR in the OB26 grating were taken as representative of the entire sample. The parameters were perturbed by ±100 K, ±0.6 dex, ±0.20 dex and ±0.25 dex for T_{eff}, log(g), [Fe/H] and v_t respectively. These were chosen so as to contain $\sim$ 68% of the variation between the photometric and spectroscopic temperatures within the perturbation step for T_{eff}. A similar argument is made in the choice of the perturbation step in in log(g), [Fe/H] and v_t where $\sim$ 68% of the variation between the reported values and observed values fall within our step size. We neglect the correlations between the stellar parameters and approximate them to be independent of each other. So the error due to model atmosphere, σ_{atm}, is given by the quadratic sum of the errors in the individual parameters:

$$\sigma_{atm} = \sqrt{\sigma^2_{T_{eff}} + \sigma^2_{log(g)} + \sigma^2_{[Fe/H]} + \sigma^2_{v_t}} \tag{4.2}$$

where $\sigma_{T_{eff}}$, $\sigma_{log(g)}$, $\sigma_{[Fe/H]}$, σ_{v_t} are the normailsed errors due to uncertainties in the stellar: temperature, surface gravity, metallicity and micro-turbulence velocity respectively.

The total abundance error is given by:

$$\sigma_{total} = \sqrt{\sigma^2_{meas} + \sigma^2_{atm}} \tag{4.3}$$

These uncertainties are reported in Table 4.2. The error in most of the element abundances is less than 0.20 dex and can be summarised as follows:

- The Ca abundance shows the least dependence with stellar parameter uncertainty.

Table 4.2: Uncertainties due to stellar parameters

Abundances	T_{eff} ±100K	log(g) ±0.6 dex	[Fe/H] ±0.20 dex	v_t ±0.25 km s^{-1}	σ_{atm} dex	σ_{meas} dex	σ_{total} dex
[Fe I/H]	±0.1	±0.01	±0.01	∓0.11	0.15	0.03	0.15
[Fe II/H]	∓0.1	±0.28	±0.07	∓0.07	0.31	0.17	0.35
[Si I/Fe I]	∓0.12	±0.08	±0.02	±0.1	0.17		0.17
[Ca I/Fe I]	±0.02	∓0.05	∓0.02	±0.03	0.06	0.1	0.12
[Ti I/Fe I]	±0.09	∓0.02	∓0.03	±0.01	0.1	0.11	0.15
[Ti II/Fe II]	±0.08	∓0.06	∓0.02	∓0.09	0.13		0.13
[Cr I/Fe I]	±0.06	∓0.03	∓0.02	±0.01	0.07	0.4	0.41
[Y II/Fe II]	±0.1	∓0.05	∓0.01	∓0.04	0.12	0.11	0.16
[Ce II/Fe II]	±0.11	∓0.04	±0.01	±0.05	0.13		0.13
[Nd II/Fe II]	±0.12	∓0.04	∓0.01	±0.03	0.13	0.05	0.14
[Er II/Fe II]	±0.17	∓0.05	∓0.02	∓0.01	0.18		0.18

- The abundance relations of Cr I and Fe II show huge errors. The Cr abundance is limited by the measurement uncertainty while Fe II is limited by stellar parameter uncertainty.

- Effective temperature (T_{eff}) is found to be the dominating factor in the σ_{atm} for most elements except for Fe II.

- Fe II is affected more by log(g). This is due to the dependence of the Fe II on electron pressure which is sensitive to log(g).

Table 4.3 compares the abundance dependencies with stellar parameters between this work and Ivans et al. (2001). Note that Ivans et al. (2001) use a smaller perturbation step than our study and care has been taken to characterize the uncertainties of this work with the same perturbation steps for comparison purposes. There is a good overall agreement of the model atmosphere uncertainties with Ivans et al. (2001).

Table 4.4: Signal-to-noise ratio seen in the OB26 setting (λ 6627Å) for the observed stars

Star ID:	SNR
15184164 + 0203533	62.193

Table 4.4 – *Continued from previous page*

Star ID:	SNR
15183505 + 0201068	51.751
15182262 + 0200305	60.861
15183583 + 0203421	74.889
15182938 + 0208275	58.22
15182717 + 0159524	59.607
15183223 + 0201341	51.598
15182324 + 0159163	53.589
15180537 + 0202015	65.933
15180892 + 0206285	50.214
15182345 + 0159572	60.123
15184449 + 0202053	44.249
15184001 + 0211023	52.196
15182594 + 0203108	60.063
15184120 + 0201511	52.364
15183693 + 0204389	34.348
15184052 + 0207337	39.161
15180407 + 0205557	45.989
15190237 + 0204586	20.582
6	21.997
15183463 + 0209313	39.134
15183815 + 0203219	28.376
15182624 + 0205545	40.613
15183481 + 0202226	29.069
15185420 + 0205473	26.775
1	26.096
15184114 + 0205528	33.106

Table 4.4 – *Continued from previous page*

Star ID:	SNR
15182581 + 0204552	27.68
15183182 + 0203277	25.452
15184730 + 0207253	23.434
15181172 + 0202519	44.47
15183086 + 0212167	28.598
15183638 + 0208507	36.948
15183050 + 0209224	25.103
15184864 + 0205290	32.255
15184833 + 0206520	20.296
15184734 + 0202509	28.988
15185731 + 0203077	23.751
15182575 + 0201461	47.296
15183978 + 0201101	26.69
15182072 + 0206414	33.592
15181418 + 0201222	25.38
15181803 + 0203503	25.346
15183326 + 0207248	27.556
15181644 + 0207177	22.949
15181126 + 0206347	25.835
15183280 + 0204362	40.963
15182634 + 0206502	18.251
15182245 + 0202242	33.813
15182347 + 0203489	29.494
15184233 + 0207406	25.5
36	13.007
15184866 + 0209472	17.161

Table 4.4 – *Continued from previous page*

Star ID:	SNR
15182264 + 0210037	14.834
15181445 + 0203131	27.357

Table 4.3: Comparison of abundance dependencies with stellar parameter between Ivans et al. (2001) (1) and this work (2) with errors recomputed using the same perturbation step for comparison purpose only.

Abundances	[Fe I/H]	[Fe II/H]	[Si I/Fe I]	[Ca I/Fe I]	[Ti I/Fe I]	[Ti II/Fe II]
ΔT_{eff} [1] ±50 K	±0.04	∓0.06	∓0.06	±0.02	±0.06	±0.04
ΔT_{eff} [2] ±50 K	±0.05	∓0.05	∓0.06	±0.01	±0.04	±0.04
$\Delta \log(g)$ [1] ±0.20 dex	±0.02	±0.11	±0.02	∓0.03	∓0.03	∓0.02
$\Delta \log(g)^2$ ±0.20 dex	±0	±0.09	±0.03	∓0.02	∓0	∓0.02
Δv_t [1] ±0.20 dex	∓0.09	∓0.04	±0.08	±0.01	±0.03	±0.01
Δv_t^2 ±0.20 dex	∓0.09	∓0.06	±0.08	±0.02	±0	∓0.07
Δ [Fe/H][1] ±0.20 dex	±0.02	±0.08	∓0.02	±0.03	±0.03	∓0.07
Δ [Fe/H][2] ±0.20 dex	±0.01	±0.07	±0.02	∓0.02	∓0.03	∓0.02

5

Discussion

5.1 Variation of [Fe/H] with Stellar Parameters

The average value of T_{eff} among the stars in this study is 4673 K. The iron abundance exhibits a very small anti-correlation with T_{eff} with a slope of -2.7×10^{-4} with an asymptotic error of $\pm 9.86 \times 10^{-5}$. This is an artificial trend which arises due to the uncertainty in the iron abundance. There is a huge spread in the iron abundance observed in this study which is neither observed in the literature (Carretta et al. 2009b) nor in the HRD of M5. The increased spread in iron abundances among the warmer stars in this study (see Figure 5.1) is probably due to the lower SNR seen in their spectra.

There is a correlation seen in variation of [Fe/H] with $\log(g)$ with the gradient being 0.232 ± 0.038. To derive the iron abundance we use six Fe II lines and 82 Fe I lines (see Table 2.1). The scatter in iron abundance is due to the stellar parameter uncertainties specifically the surface gravity which greatly affects Fe II abundance. This is can be due to $\log(g)$ being taken as a free parameter or the breaking of the LTE condition in some AGB and post-AGB stars. Instead of keeping $\log(g)$ as a free parameter we can derive it using the photometric luminosity as shown in Ivans et al. (2001) but at the expense of the deriving it independently without any assumptions of the stellar mass. Increasing the number of Fe II lines could also help in getting a better estimate of the

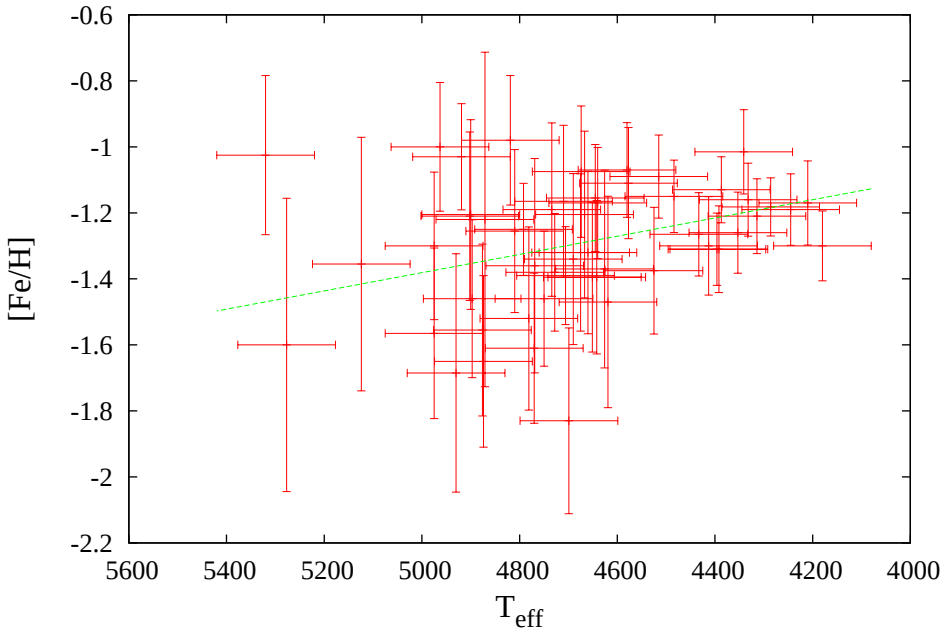

Figure 5.1: Plot of [Fe/H] versus T_{eff} with a linear fit.

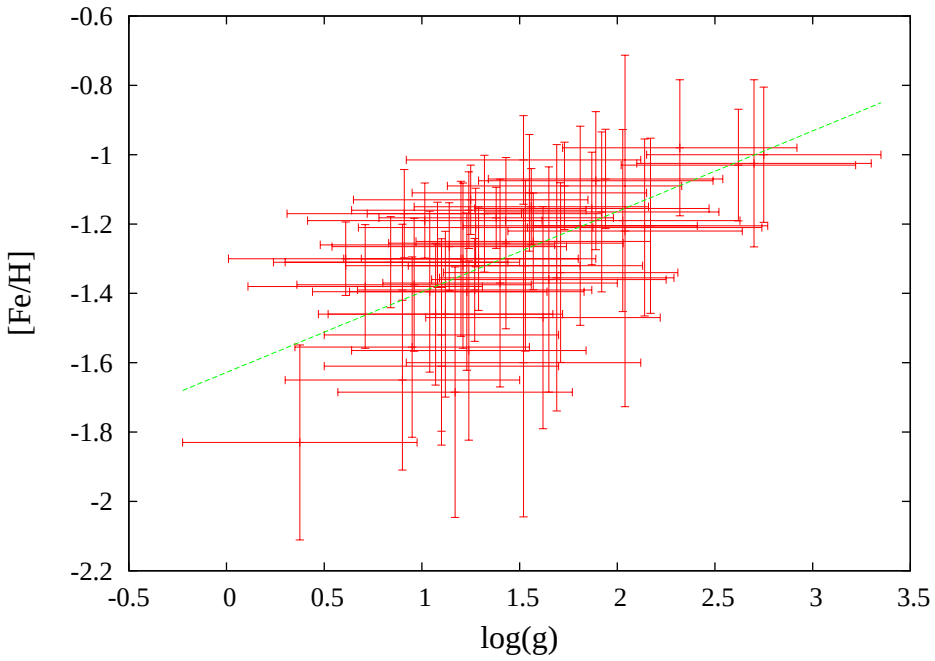

Figure 5.2: Plot of [Fe/H] versus log(g) with a linear fit.

iron abundances.

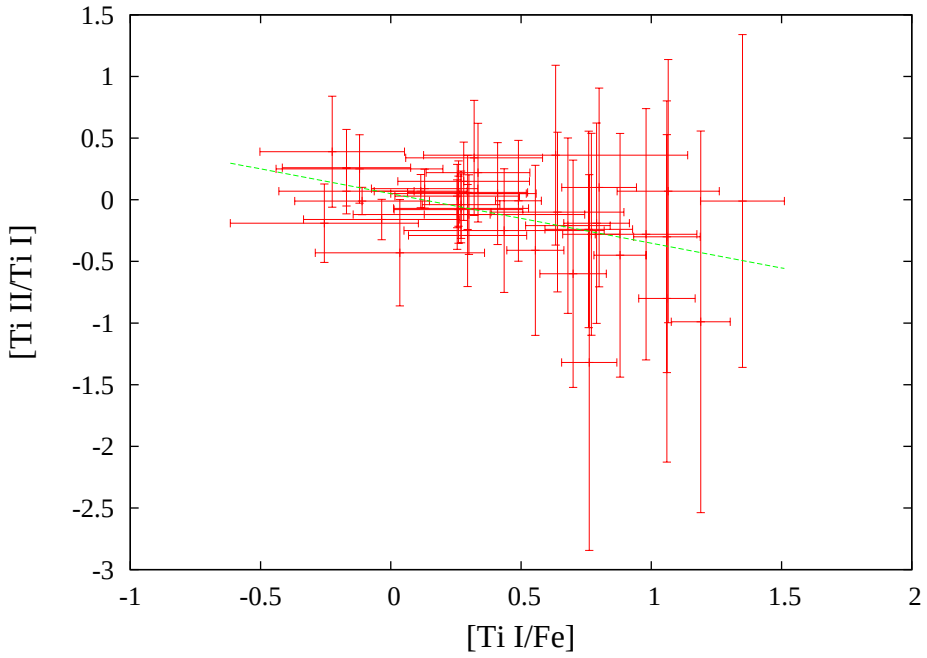

Figure 5.3: Plot of [Ti II/Ti I] versus [Ti I/Fe] with a linear fit.

5.2 Determining the correctness of model atmospheres using Titanium abundance

The correctness of the model atmospheres (thereby stellar parameters) can be checked by knowing the [Ti II/Ti I] abundance. Since we imposed ionization equilibrium in our stellar parameters there should be no difference between the two titanium abundances measured. Therefore we expect to see a perfect correlation between [Ti I/Fe] and [Ti II/Fe] but from Figure 5.3 we see a a slope of -0.041 ± 0.115 when we expect a flat line of no slope.

When we plot [Ti II/Ti I] with T_{eff} we find that stars with T_{eff} between 4600 K and 5000 K show an acceptable scatter around the expected value of zero. The stars with low T_{eff} (less than 4300 K) show a huge mismatch in their titanium abundance thus signifying their faulty stellar parameters.

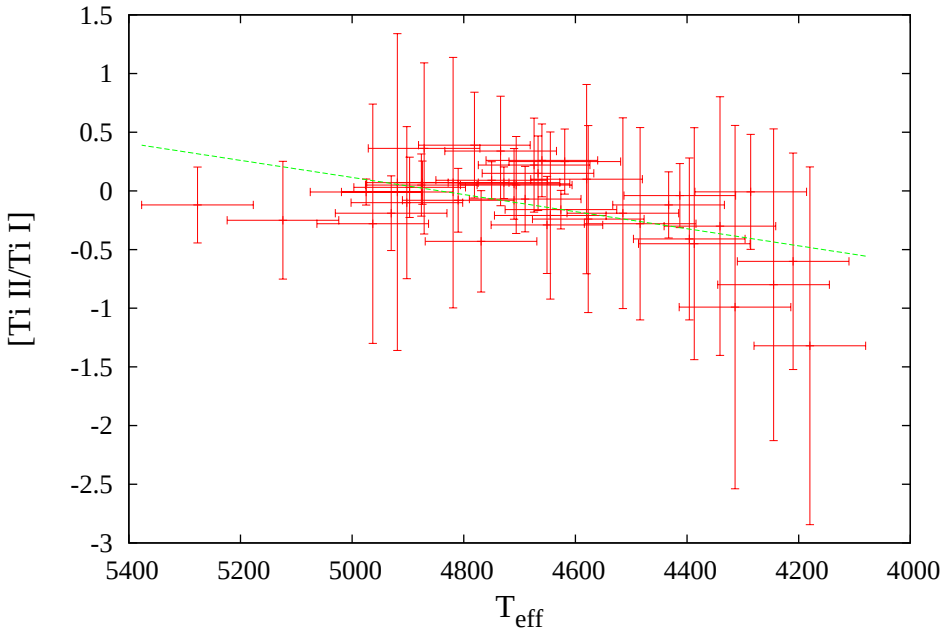

Figure 5.4: Plot of [Ti I/Ti II] versus T_{eff}

5.3 Variation of abundance with radial distance

The distance of the star from the cluster centre is calculated using the ASDC angular distance calculator [1]. The cluster centre has the co-ordinates of RA=$15^h18^m33.22^s$, Dec=+02°04′51.7″ (Harris 2010). Figure 5.5 shows the distribution of projected distances in this study. The stellar distances vary from 0.28 to 23 arcminutes from the cluster centre. The distribution of distances is a combination of actual stellar density convolved with how closely the fibres can be placed in the spectrograph. The stars with distances greater than 8 arcminutes are avoided in the further discussion in this section.

Iron abundance

The iron abundance is plotted against distance from cluster centre in Figure 5.6. The slope of the linear fit is -0.008 ± 0.0152. Overall iron abundance does not show any

[1] URL:`http://www.asdc.asi.it/dist.html`

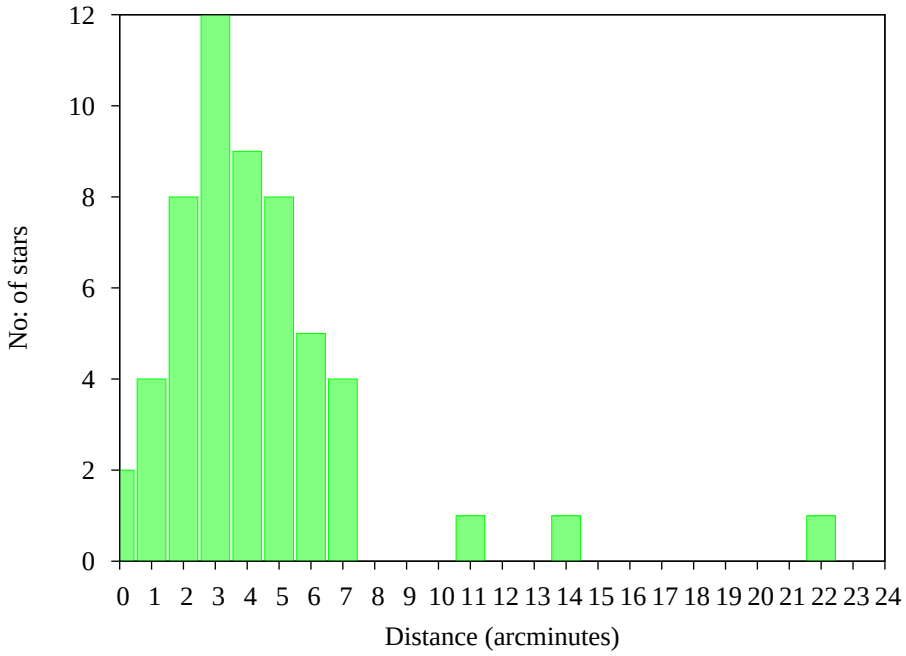

Figure 5.5: Histogram showing distribution of projected distances from the cluster centre

trend with the projected distance from cluster centre.

Silicon

The silicon abundance, [Si/Fe], shows much less spread in its variation with cluster distance. The linear fit has a slope of 0.017 ± 0.027. Due to the uncertainty being of the same order as the slope, the trend is considered to be statistically insignificant. The [Si/Fe] is considered to show no variation with cluster distance as seen in Figure 5.7.

Calcium

This shows a similar behaviour as [Si/H]. The linear fit has a slope of 0.003 ± 0.01 (see Figure 5.8). Due to the large fractional uncertainty in the slope, it can be neglected. Again there is no significant variation seen with respect to distance from the cluster centre.

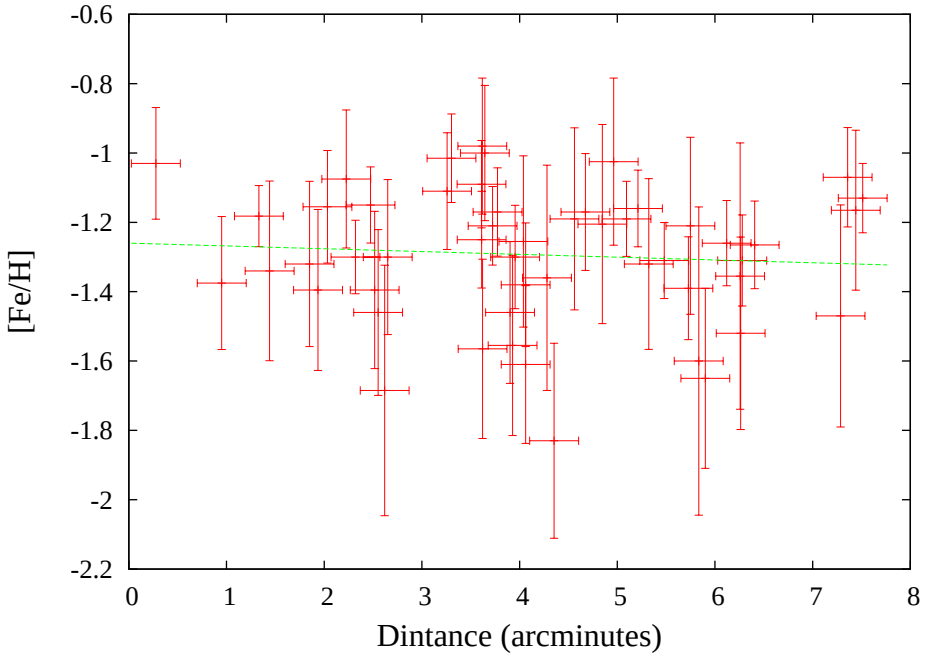

Figure 5.6: Plot of [Fe/H] versus projected distance from cluster centre with a linear fit.

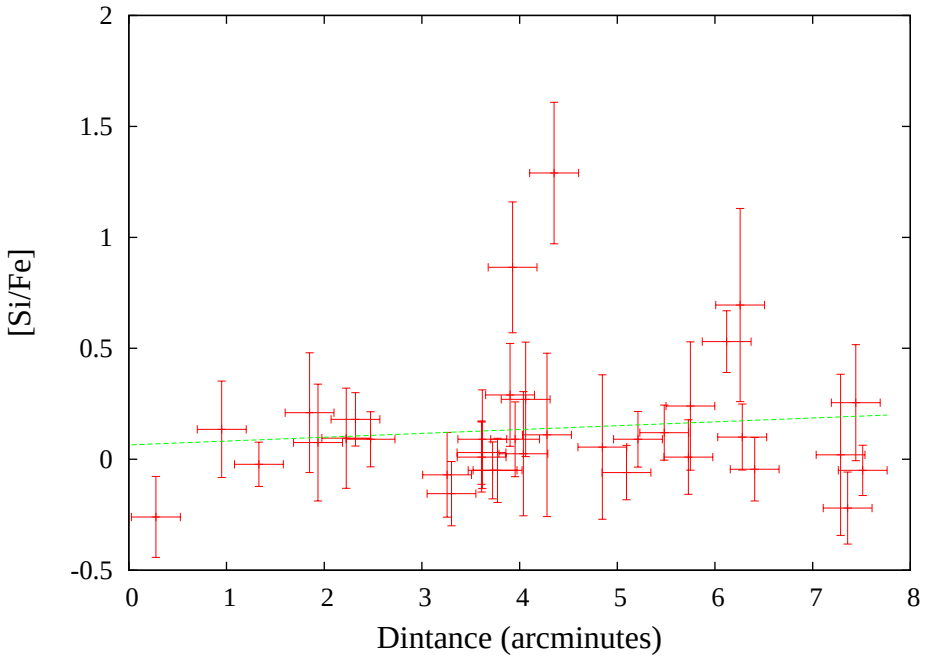

Figure 5.7: Plot of [Si/Fe] versus projected distance from cluster centre with a linear fit.

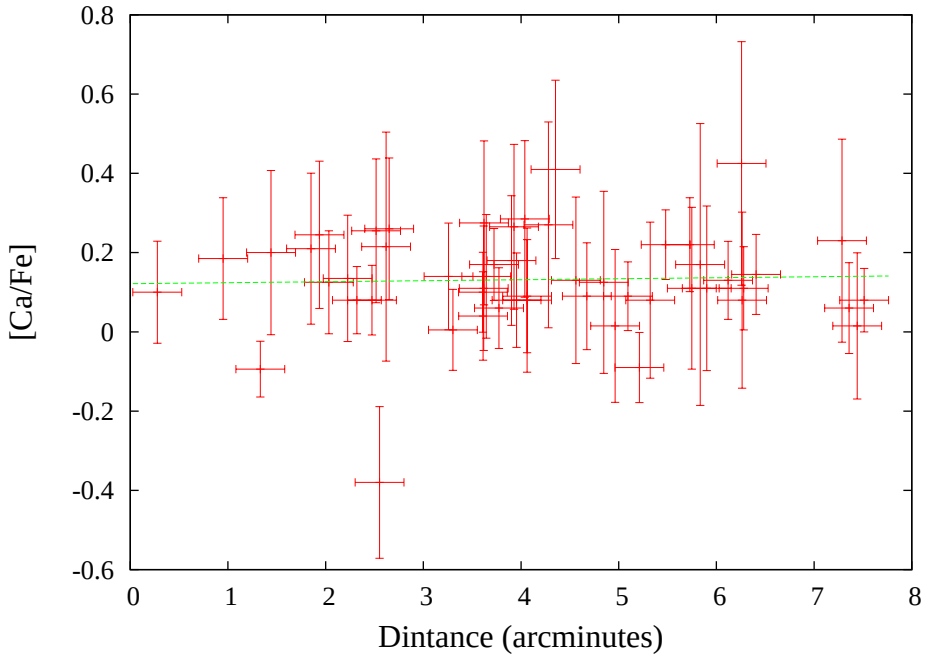

Figure 5.8: Plot of [Ca/Fe] versus distance from cluster centre with a linear fit.

Titanium

Figure 5.9 shows the [Ti I/Fe] variation with distance from cluster centre. There is a big spread in the abundance values between 3 and 5 arcminutes due to more number of stars sampled in this region. The linear fit shows a slope of 0.002 ± 0.019. There is no real trend of [Ti I/Fe] with distance in M5.

The [Ti II/Fe] shows a bigger spread than [Ti I/Fe] values (see Figure 5.10). The linear fit has a gradient of 0.019 ± 0.019. There is no real variation seen with distance.

α-Elements

The combined behaviour of silicon, calcium and titanium is reflected in the α-element abundance. The α-elements show a similar variation as [Si/Fe] with distance albeit with much lesser spread. The linear fit has a slope of 0.008 ± 0.011. The result confirms the absence of any real trend in the [α/Fe] variation with distance.

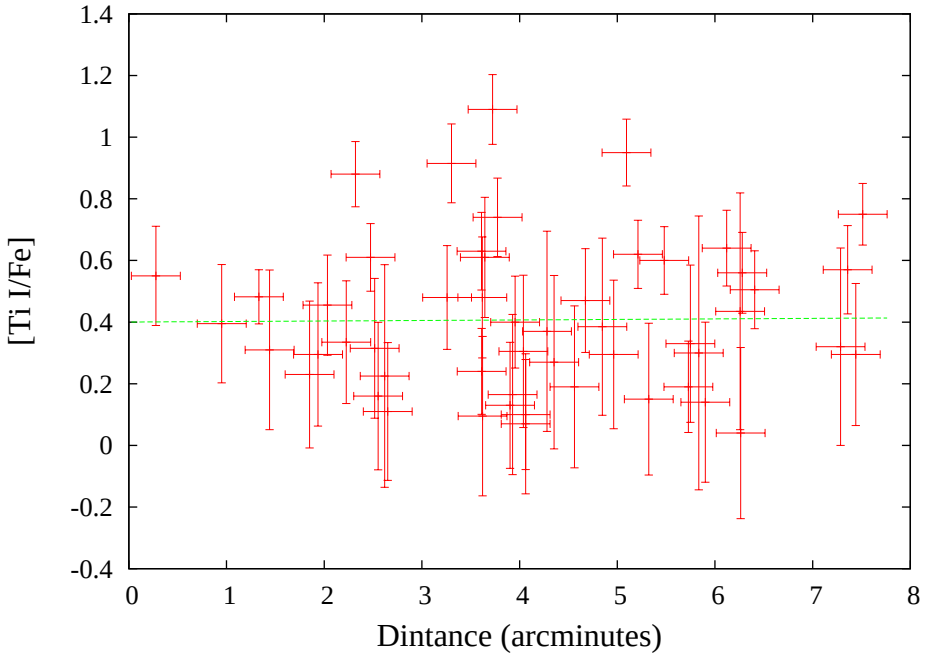

Figure 5.9: Plot of [Ti I/Fe] versus projected distance from cluster centre with a linear fit.

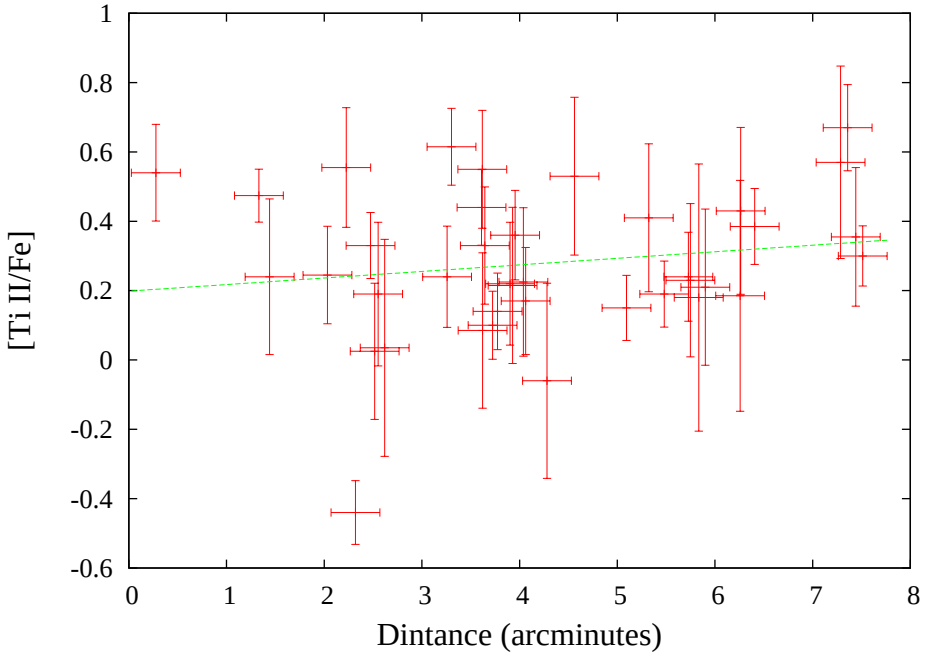

Figure 5.10: Plot of [Ti II/Fe] versus distance from cluster centre with a linear fit.

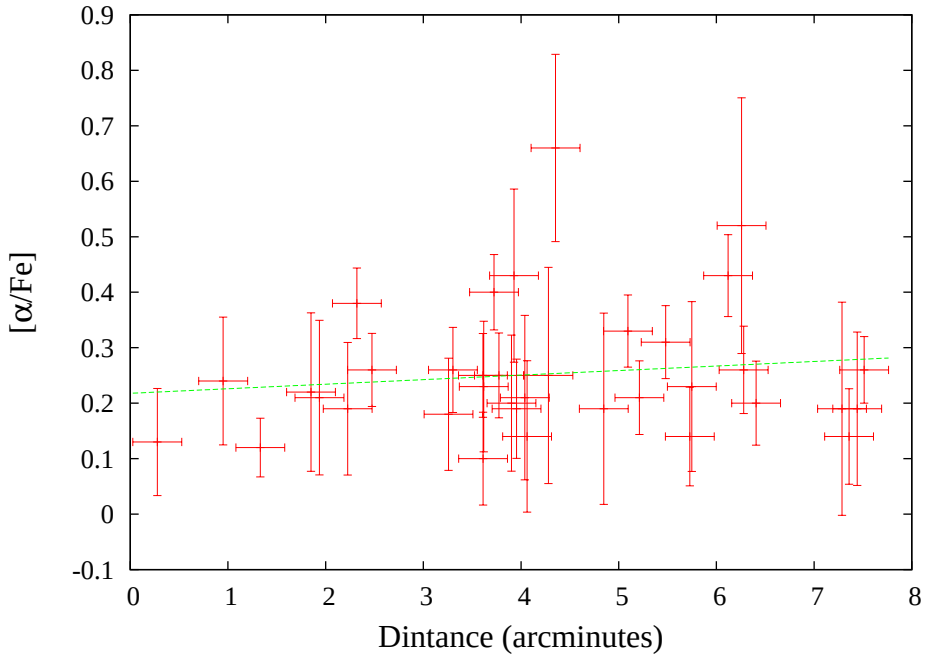

Figure 5.11: Plot of [α/H] versus distance from cluster centre with a linear fit.

Other elements

Figures 5.12, 5.13, 5.14, 5.15, 5.16 shows the variation of [Cr/Fe], [Y/Fe], [Ce/Fe], [Nd/Fe] and [Er/Fe], respectively. The corresponding gradients seen in them are 0.019 ± 0.015, -0.017 ± 0.02, -0.008 ± 0.02, -0.014 ± 0.021 and -0.097 ± 0.062, respectively. The corresponding slopes are statistically insignificant due to high relative uncertainty in them. Therefore no real trends are seen in the variation of any element with distance.

5.4 Comparison with photometry

The effective temperatures obtained from MOOG (Section 2.3.3) are compared with the photometric temperatures of M5 from McDonald et al. (in preparation). The photometry values were derived from several sources:

- Optical UBVRI photometry are taken from Viaux et al. (2013).
- Optical g- and i-band photometry from Sloan et al. (in prep.).

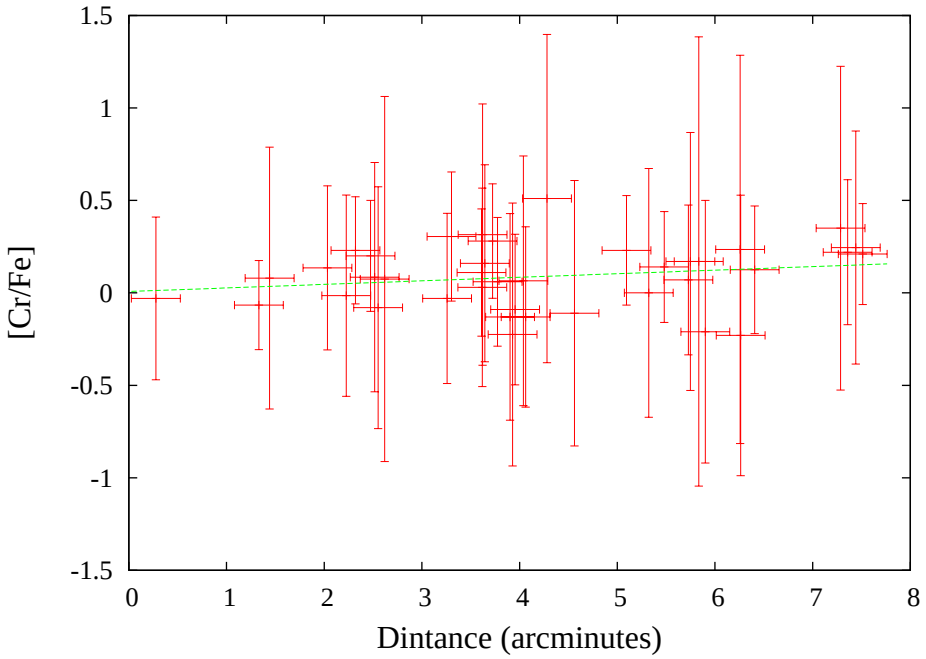

Figure 5.12: Plot of [Cr/Fe] versus distance from cluster centre with a linear fit.

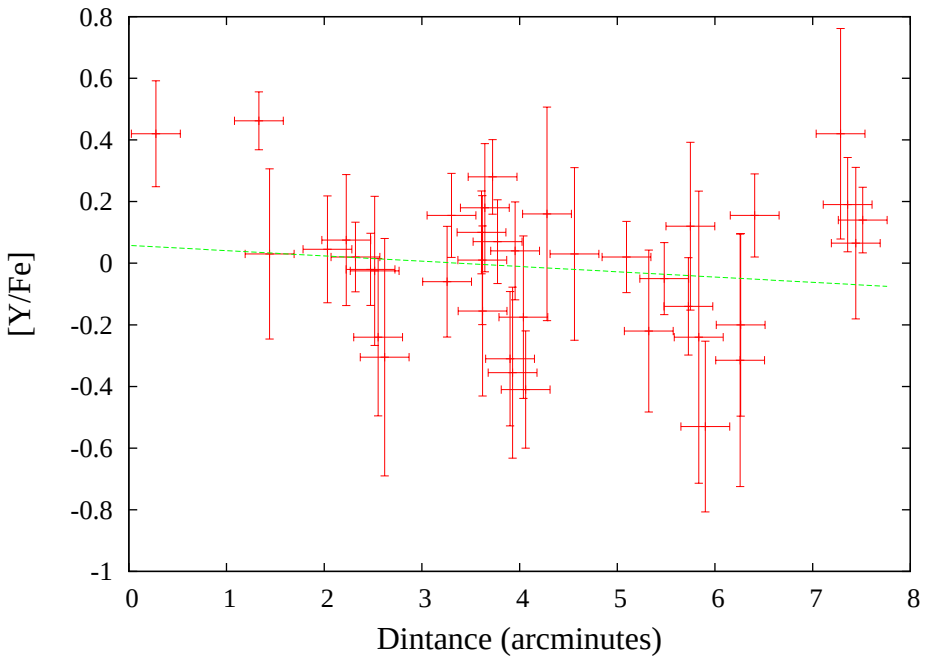

Figure 5.13: Plot of [Y II/Fe] versus distance from cluster centre with a linear fit.

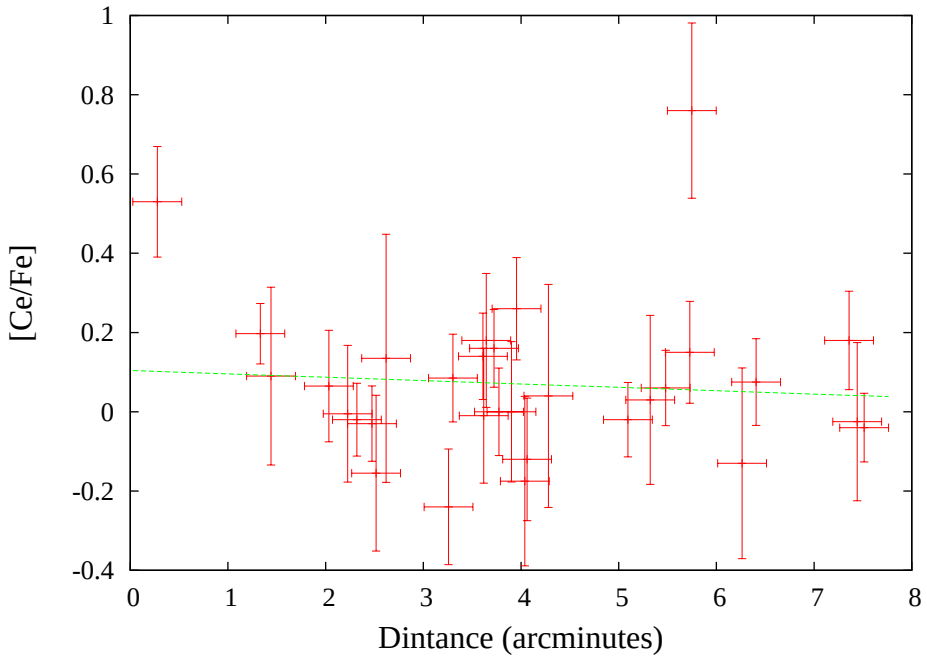

Figure 5.14: Plot of [Ce II/Fe] versus distance from cluster centre with a linear fit.

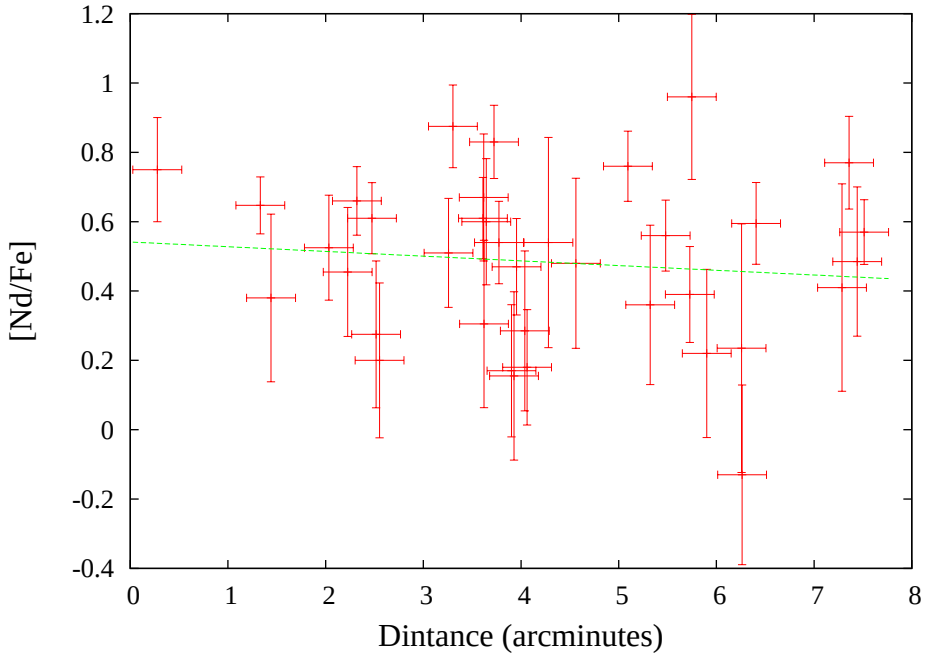

Figure 5.15: Plot of [Nd II/Fe] versus distance from cluster centre with a linear fit.

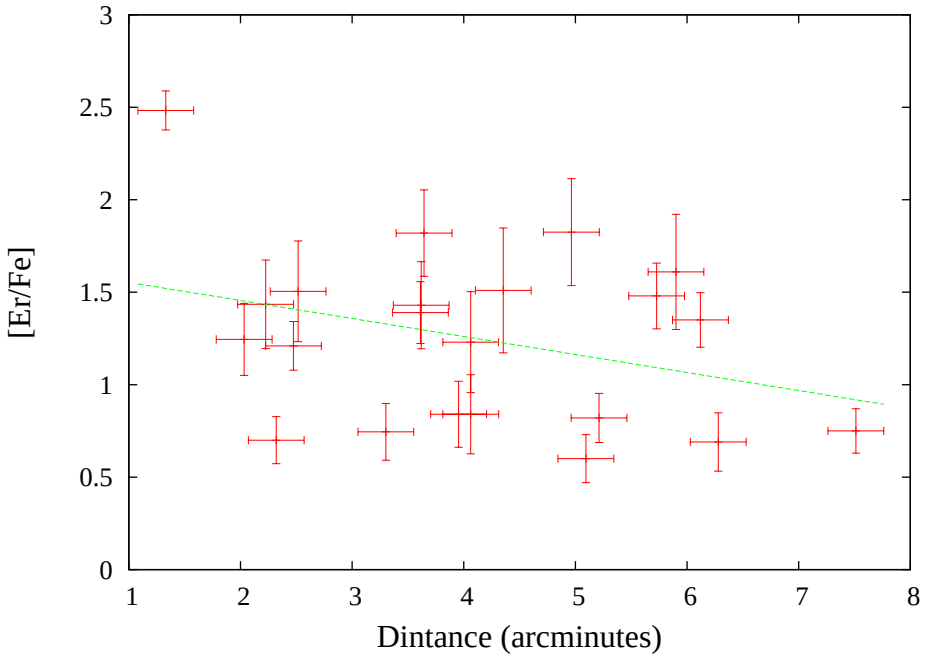

Figure 5.16: Plot of [Er II/Fe] versus distance from cluster centre with a linear fit.

- Near-infrared photometry from 2MASS Cutri et al. (2003).
- Near-infrared photometry from Valenti et al. (2004).
- Archival mid-infrared photometry from the *Spitzer Space Telescope*, reduced by Martha Boyer.

These were combined using the spectral-energy distribution fitting method described in McDonald et al. (2012). Effective temperatures and luminosities were calculated assuming [Fe/H] = −1.29 dex, a stellar mass of 0.80 $M_{\odot}$, a distance of 7.5 kpc, and interstellar reddening of E(B-V) = 0.03 mag following the reddening law used in McDonald et al. (2012).

The differences are tabulated in Table 5.1. On average the spectroscopic temperatures are ∼ 33 K higher with respect to the photometric ones. There is also a large variation in the Δ T_{eff} value with the standard deviation being 213 K. Three stars in particular show huge differences between their photometric and spectroscopic temperatures: 15182245+0202242 ($\Delta T_{eff}^{spect.-phot.}$=396 K, 15183280+0204362 ($\Delta T_{eff}^{spect.-phot.}$=525 K)

and 15181445+0203131 ($\Delta T_{eff}^{spect.-phot.}$=1083 K). These stars may be photometrically confused. Ignoring them, we find the new average and standard deviation in $\Delta T_{eff}^{spect.-phot.}$ of −4 K and 132 K. The photometric error These results show a good agreement between the two values. These errors are consistent with other errors in the stellar parameters.

Table 5.1: Comparison between photometric and spectroscopic temperatures

Star	L_{phot}	T_{eff}^{phot}	$T_{eff}^{spec.}$	$\Delta T_{eff}^{spec-phot}$	Our Classification
	$L_\odot$	K	K	K	
15180407+0205557	438.056	4421	4580	159	RGB
15180537+0202015	730.433	4244	4387	143	RGB
15180892+0206285	540.647	4339	4392	53	RGB
15181126+0206347	146.064	4740	4902	162	RGB
15181172+0202519	269.858	4732	4706	−26	AGB
15181418+0201222	115.529	5122	4874	−248	AGB
15181445+0203131	117.096	4237	5320	1083	Not classified
15181644+0207177	135.848	4766	4900	134	RGB
15181803+0203503	129.601	5106	4876	−230	AGB
15182072+0206414	206.496	4677	4819	142	RGB
15182245+0202242	216.787	4567	4963	396	Not classified
15182262+0200305	991.588	4135	4245	110	RGB
15182264+0210037	72.1805	5389	5277	−112	AGB
15182324+0159163	567.648	4335	4353	18	RGB
15182345+0159572	640.862	4289	4396	107	RGB
15182347+0203489	133.276	5041	4975	−66	AGB
15182575+0201461	326.741	4679	4792	113	AGB
15182581+0204552	155.74	4729	4675	−54	RGB
15182594+0203108	554.753	4373	4484	111	RGB
15182624+0205545	324.85	4496	4645	149	RGB

Table 5.1 – *Continued from previous page*

Star	L_{phot}	T_{eff}^{phot}	$T_{eff}^{spec.}$	$\Delta T_{eff}^{spec-phot}$	Our Classification
	$L_{\odot}$	K	K	K	
15182634+0206502	86.9586	5133	4930	−203	AGB
15182717+0159524	662.396	4283	4332	49	RGB
15182938+0208275	1285.96	4037	4314	277	RGB
15183050+0209224	137.477	4786	4734	−52	RGB
15183086+0214167	215.922	4632	4710	78	RGB
15183182+0203277	137.17	4755	4690	−65	RGB
15183223+0201341	874.366	4188	4341	153	RGB
15183280+0204362	325.042	4394	4919	525	Not classified
15183326+0207248	132.336	5039	4897	−142	AGB
1	230.074	4626	4667	41	RGB
15183463+0209313	335.603	4539	4640	101	RGB
15183481+0202226	168.338	4705	4651	−54	RGB
15183505+0201068	877.847	4202	4210	8	RGB
15183583+0203421	1260.77	4081	4286	205	RGB
15183638+0208507	237.722	4858	4728	−130	AGB
15183693+0204389	275.877	4550	4525	−25	RGB
15183815+0203219	181.796	4669	4642	−27	RGB
15183978+0201101	247.097	4832	4810	−22	AGB
15184001+0211023	455.865	4415	4433	18	RGB
15184052+0207337	361.031	4479	4577	98	RGB
15184114+0205528	224.254	4636	4674	38	RGB
15184120+0201511	512.764	4399	4515	116	RGB
15184164+0203533	1142.56	4115	4180	65	RGB
15184233+0207406	160.684	5127	4975	−152	AGB
15184449+0202053	412.708	4453	4413	−40	RGB

Table 5.1 – *Continued from previous page*

Star	L_{phot}	T_{eff}^{phot}	$T_{eff}^{spec.}$	$\Delta T_{eff}^{spec-phot}$	Our Classification
	$L_\odot$	K	K	K	
15184730+0207253	190.318	4942	4699	−243	AGB
15184734+0202509	177.067	4947	4770	−177	AGB
15184833+0206520	109.695	4647	4769	122	RGB
15184864+0205290	214.26	4861	4750	−111	AGB
15184866+0209472	102.595	5208	5124	−84	AGB
15185420+0205473	139.385	4785	4660	−125	RGB
15185731+0203077	135.448	5080	4781	−299	AGB
15190237+0204586	103.993	4791	4619	−172	RGB
6	181.833	4713	4626	−87	RGB
36	99.1866	4907	4871	−36	RGB
Average	**349**	**4641**	**4673**	**33**	

5.5 Variation between AGB and RGB star mass

The typical mass of an RGB star is ∼0.84 $M_\odot$ (McDonald and Zijlstra 2015b) while the mass of an AGB star is typically ∼0.63 $M_\odot$ (Gratton et al. 2010b). Hence we should expect the AGB star masses to be ∼25% lower than the RGB stellar masses. We follow a similar procedure to that outlined in McDonald et al. (2011) to differentiate between AGB and RGB stars based on their masses using:

$$M = \frac{gL}{4\pi\sigma T_{eff}^4 G} \tag{5.1}$$

where g is the surface gravity (spectroscopic), L is the stellar luminosity, σ is the Stefan-Boltzmann constant, T_{eff} is the effective temperature (photometric) and G is

the gravitational constant. This can be modified to:

$$\frac{M}{M_{\odot}} = \frac{(g/g_{\odot})(L/L_{\odot})}{(T_{eff}/T_{\odot})^4} \tag{5.2}$$

to obtain stellar mass in solar units. The T_{eff} used is the average of photometric and spectroscopic temperature, the value of $\log(g)_{\odot}$ is taken to be 4.44 cm s^{-2} and $T_{\odot}$ is taken to be 5778 K. Figure 5.17 shows the CMD of our sample (excluding the three stars which are considered to be photometrically confused) prepared using data from McDonald et al.(in preparation). The RGB and AGB are spearated by eye inspection as it shows a well separated branches. We would like to find the masses of these stars and find how they vary in the RGB and AGB. Figure 5.18 shows the variation of derived masses of AGB and RGB. The average mass of RGB is 1.44 $M_{\odot}$ while the AGB average mass is 0.22 $M_{\odot}$. The average error in the mass is 0.66 and 0.12 $M_{\odot}$, respectively. This indicates a huge error in mass and hence not used to calculate the mass loss during the RGB evolution. However despite the error in absolute masses we can see a distinction between RGB and AGB stars in Figure 5.18. There's a systematic over-prediction of T_{eff} from spectrocopy for RGB stars while AGB stars show an under-prediction. The average value of ΔT_{eff} between spectroscopy and photometry for RGB and AGB stars is 63 K and -133 K, respectively. This could systematic offset could be responsible for the huge errors seen in the derived masses.

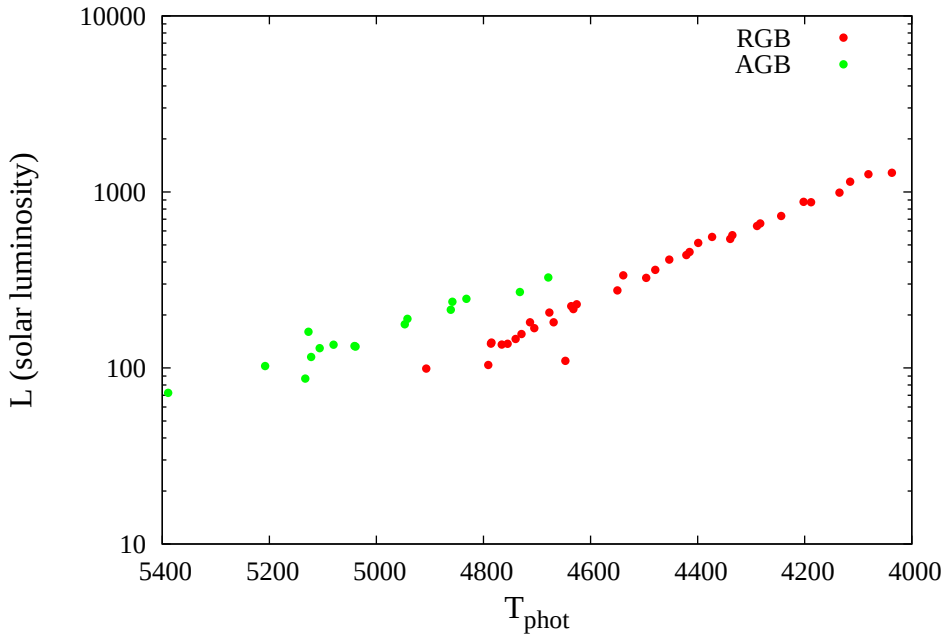

Figure 5.17: CMD of sample stars. RGB star are represented by red while AGB stars are represented by green.

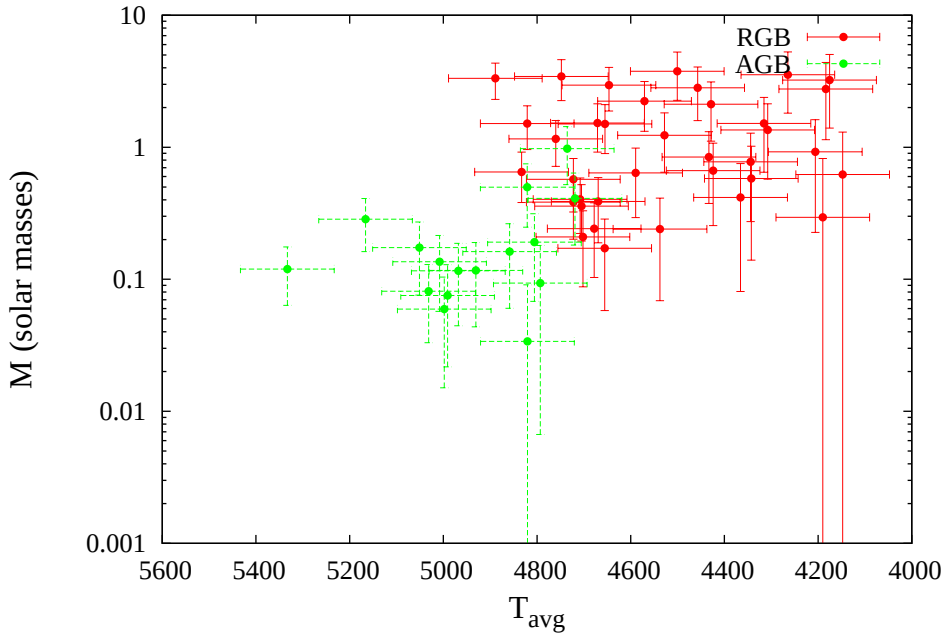

Figure 5.18: Variation of derived mass for RGB (red) and AGB (green)

6

Conclusion

The Stellar parameters and iron abundances are found for 55 stars (AGB and RGB) in the galactic globular cluster M5. We also report the abundances of silicon, calcium, titanium, chromium, yttrium, cerium, neodymium, and erbium. The cluster averages for the present sample in tabulated in Table 6.1. The average iron abundance is found to be consistent with the reported values. A spread in the iron abundance is noted for this sample of stars. This is due to the low SNR in the spectra. A correlation is seen between [Fe/H] and log(g) which suggests that surface gravity obtained might not be accurate for all the star in this sample. We verify the correctness of the stellar parameters by checking for the ionization equilibrium betwee Ti I and Ti II. We see systematic error in [Ti I/Ti II] for stars with T_{eff} lower than 4400 K.

The best comparisons of with the literature is given in the following list:

- The [Si/Fe] found in this study is 0.05 dex lower than Lai et al. (2011).
- [Ca/Fe] is 0.13 dex lower than Ivans et al. (2001).
- [Ti I/Fe] is 0.18 dex higher than Ivans et al. (2001).
- [Ti II/Fe] is consistent with Lai et al. (2011).
- [Cr/Fe] 0.17 dex higher than Lai et al. (2011).

Table 6.1: Average values of [X/Fe] found in this study. Note the iron abundances are given relative to H.

Element	Value dex	σ_{tot} dex
Fe I	−1.29	±0.15
Fe II	−1.29	±0.35
Si	0.16	±0.17
Ca	0.13	±0.12
Ti I	0.4	±0.15
Ti II	0.31	±0.13
Cr	0.10	±0.41
Y	0.01	±0.16
Ce	0.13	±0.13
Nd	0.52	±0.14
Er	1.27	±0.18

- [Y/Fe] is 0.21 dex higher than Lai et al. (2011).
- [Ce/Fe] is 0.23 dex higher than Lai et al. (2011).
- [Nd/Fe] is 0.47 dex higher than Lai et al. (2011).

An anti-correlation is seen with iron abundance for all the other elements. This is not reported in any of the previous studies and is considered to be artificial, arising due to the [Fe/H] spread. It would be interesting to further study the abundance variation of other α-elements such as Mg and Na. No trend is observed between any of the abundance ratios with the projected distance from the cluster centre.

The spectroscopic temperature obtained is found to be comparable to the photometric temperatures with a few exceptions. On average, the spectroscopic temperatures are 33 K higher than the photometric temperatures for the entire smaple.

The derived masses of the RGB and AGB stars are not accurate enough to calculate the mass loss in the RGB evolution. The systematic offset between the photometric and spectroscopic temperature may be the cause of the uncertainty. The average difference between the spectroscopic and photometric temperatures for RGB and AGB stars

based on our classification is 63 K and −133 K respectively. However we can still see a distinction between the RGB and AGB stars the derived mass plot.

Although we were not able to study the variation of element abundances among individual stars, due to the lack to high signal-to-noise ratio in the spectra, we find reasonably accurate cluster averages for certain elements which agree with the literature. Our accuracy could be increased by determining stellar surface gravity (log(g)) from photometry and using non-LTE methods. Increasing the number of Fe II lines could also help in reducing the scatter in iron abundances. A enhancement of α-elements is not clearly seen in our work and it would be interesting to investigate the abundances of other $alpha$-elements such as magnesium (Mg), aluminium (Al), sodium (Na) and oxygen (O) in our sample. The presence of α-enhancement would hint strongly at the presence of second-generation AGB stars in M5.

References

K. M. Ashman and S. E. Zepf. *Globular Cluster Systems*. May 1998.

M. Asplund, N. Grevesse, A. J. Sauval, and P. Scott. The Chemical Composition of the Sun. *ARA&A*, 47:481–522, September 2009.

L. R. Bedin, G. Piotto, J. Anderson, I. R. King, S. Cassisi, and Y. Momany. The double main sequence of Omega Centauri. *Memorie della Societa Astronomica Italiana Supplementi*, 5:105, 2004.

T. C. Beers and N. Christlieb. The Discovery and Analysis of Very Metal-Poor Stars in the Galaxy. *Annual Review of Astronomy and Astrophysics*, 43:531–580, September 2005.

J. Binney and S. Tremaine. *Galactic dynamics*. 1987.

J. P. Brodie and J. Strader. Extragalactic Globular Clusters and Galaxy Formation. *Annual Review of Astronomy and Astrophysics*, 44:193–267, September 2006.

A. Burkert, J. W. Truran, and G. Hensler. The collapse of our Galaxy and the formation of the Galactic disk. *Astrophysical Journal*, 391:651–658, June 1992.

S. W. Campbell, V. D'Orazi, D. Yong, T. N. Constantino, J. C. Lattanzio, R. J. Stancliffe, G. C. Angelou, E. C. Wylie-de Boer, and F. Grundahl. Sodium content as a predictor of the advanced evolution of globular cluster stars. *Nature*, 498:198–200, June 2013.

M. Cantiello, N. Langer, I. Brott, A. de Koter, S. N. Shore, J. S. Vink, A. Voegler, and S.-C. Yoon. On the origin of microturbulence in hot stars. *Communications in Asteroseismology*, 158:61, July 2009.

E. Carretta, A. Bragaglia, R. Gratton, V. D'Orazi, and S. Lucatello. Intrinsic iron spread and a new metallicity scale for globular clusters. *Astronomy and Astrophysics*, 508:695–706, December 2009a.

E. Carretta, A. Bragaglia, R. G. Gratton, S. Lucatello, G. Catanzaro, F. Leone, M. Bel-

lazzini, R. Claudi, V. D'Orazi, Y. Momany, S. Ortolani, E. Pancino, G. Piotto, A. Recio-Blanco, and E. Sabbi. Na-O anticorrelation and HB. VII. The chemical composition of first and second-generation stars in 15 globular clusters from GIRAFFE spectra. *A&A*, 505:117–138, October 2009b.

E. Carretta, A. Bragaglia, R. G. Gratton, S. Lucatello, V. D'Orazi, M. Bellazzini, G. Catanzaro, F. Leone, Y. Momany, and A. Sollima. NGC 362: another globular cluster with a split red giant branch. *Astronomy and Astrophysics*, 557:A138, September 2013.

E. Carretta, R. G. Gratton, G. Clementini, and F. Fusi Pecci. Distances, Ages, and Epoch of Formation of Globular Clusters. *The Astrophysical Journal*, 533:215–235, April 2000.

F. Castelli and R. L. Kurucz. New Grids of ATLAS9 Model Atmospheres. *ArXiv Astrophysics e-prints*, May 2004.

J. G. Cohen. Abundances in globular cluster red giants. I - M3 and M13. *Astrophysical Journal*, 223:487–508, July 1978.

R. M. Cutri, M. F. Skrutskie, S. van Dyk, C. A. Beichman, J. M. Carpenter, T. Chester, L. Cambresy, T. Evans, J. Fowler, J. Gizis, E. Howard, J. Huchra, T. Jarrett, E. L. Kopan, J. D. Kirkpatrick, R. M. Light, K. A. Marsh, H. McCallon, S. Schneider, R. Stiening, M. Sykes, M. Weinberg, W. A. Wheaton, S. Wheelock, and N. Zacarias. *2MASS All Sky Catalog of point sources.* June 2003.

E. Dalessandro, D. Massari, M. Bellazzini, P. Miocchi, A. Mucciarelli, M. Salaris, S. Cassisi, F. R. Ferraro, and B. Lanzoni. First Evidence of Fully Spatially Mixed First and Second Generations in Globular Clusters: The Case of NGC 6362. *ApJL*, 791:L4, August 2014.

P. A. Denissenkov, G. S. Da Costa, J. E. Norris, and A. Weiss. The puzzling MgAl anticorrelation in globular-cluster red giants: primordial plus deep mixing scenario? *Astronomy and Astrophysics*, 333:926–941, May 1998.

A. D'Ercole, E. Vesperini, F. D'Antona, S. L. W. McMillan, and S. Recchi. Formation and dynamical evolution of multiple stellar generations in globular clusters. *MNRAS*, 391:825–843, December 2008.

J. L. E. Dreyer. A New General Catalogue of Nebulæ and Clusters of Stars, being the Catalogue of the late Sir John F. W. Herschel, Bart, revised, corrected, and enlarged. *Memoirs of thr Royal Astronomical Society*, 49:1, 1888.

D. Eggers, D. Weistrop, A. Stone, C. H. Nelson, and M. Hancock. Hubble Space Telescope Observations of Star-forming Regions in NGC 3994/3995. *The Astronomical Journal*, 129:136–147, January 2005.

S. M. Fall and M. J. Rees. A theory for the origin of globular clusters. *Astrophysical Journal*, 298:18–26, November 1985.

S. M. Fall and M. J. Rees. The origin of globular clusters. In J. E. Grindlay and A. G. D. Philip, editors, *The Harlow-Shapley Symposium on Globular Cluster Systems in Galaxies*, volume 126 of *IAU Symposium*, pages 323–330, 1988.

R. G. Gratton. Abundances in metal-poor stars. II - The anomalous globular cluster Omega Centauri. *A&A*, 115:336–346, November 1982.

R. G. Gratton, P. Bonifacio, A. Bragaglia, E. Carretta, V. Castellani, M. Centurion, A. Chieffi, R. Claudi, G. Clementini, F. D'Antona, S. Desidera, P. François, F. Grundahl, S. Lucatello, P. Molaro, L. Pasquini, C. Sneden, F. Spite, and O. Straniero. The O-Na and Mg-Al anticorrelations in turn-off and early subgiants in globular clusters. *Astronomy and Astrophysics*, 369:87–98, April 2001.

R. G. Gratton, E. Carretta, A. Bragaglia, S. Lucatello, and V. D'Orazi. The second and third parameters of the horizontal branch in globular clusters. *Astronomy and Astrophysics*, 517:A81, July 2010a.

R. G. Gratton, V. D'Orazi, A. Bragaglia, E. Carretta, and S. Lucatello. The connection between missing AGB stars and extended horizontal branches. *A&A*, 522:A77, November 2010b.

W. E. Harris. A New Catalog of Globular Clusters in the Milky Way. *ArXiv e-prints*, December 2010.

K. Hinkle, L. Wallace, J. Valenti, and D. Harmer. *Visible and Near Infrared Atlas of the Arcturus Spectrum 3727-9300 A*. 2000.

I. I. Ivans, R. P. Kraft, C. Sneden, G. H. Smith, R. M. Rich, and M. Shetrone. New Analyses of Star-to-Star Abundance Variations among Bright Giants in the Mildly Metal-poor Globular Cluster M5. *The Astronomical Journal*, 122:1438–1463, September 2001.

C. I. Johnson, I. McDonald, C. A. Pilachowski, M. Mateo, J. I. Bailey, III, M. J. Cordero, A. A. Zijlstra, J. D. Crane, E. Olszewski, S. A. Shectman, and I. Thompson. AGB Sodium Abundances in the Globular Cluster 47 Tucanae (NGC 104). *AJ*, 149:71, February 2015.

K. G. Jones. *Messier's nebulae and star clusters*. 1991.

D. K. Lai, G. H. Smith, M. Bolte, J. A. Johnson, S. Lucatello, R. P. Kraft, and C. Sneden. Chemical Abundances for Evolved Stars in M5: Lithium through Thorium. *AJ*, 141:62, February 2011.

I. McDonald, C. I. Johnson, and A. A. Zijlstra. Empirical determination of the integrated red giant and horizontal branch stellar mass-loss in ω Centauri. *MNRAS*, 416: L6–L10, September 2011.

I. McDonald and A. A. Zijlstra. Globular cluster interstellar media: ionized and ejected by white dwarfs. *Monthly Notices of the Royal Astronomical Society*, 446:2226–2242, January 2015a.

I. McDonald and A. A. Zijlstra. Mass-loss on the red giant branch: the value and metallicity dependence of Reimers' η in globular clusters. *MNRAS*, 448:502–521, March 2015b.

I. McDonald, A. A. Zijlstra, and M. L. Boyer. Fundamental parameters and infrared excesses of Hipparcos stars. *MNRAS*, 427:343–357, November 2012.

A. P. Milone, L. R. Bedin, G. Piotto, and J. Anderson. Multiple stellar populations in Magellanic Cloud clusters. I. An ordinary feature for intermediate age globulars in the LMC? *Astronomy and Astrophysics*, 497:755–771, April 2009.

A. P. Milone, L. R. Bedin, G. Piotto, J. Anderson, I. R. King, A. Sarajedini, A. Dotter, B. Chaboyer, A. Marín-Franch, S. Majewski, A. Aparicio, M. Hempel, N. E. Q. Paust, I. N. Reid, A. Rosenberg, and M. Siegel. The ACS Survey of Galactic Globular Clusters. III. The Double Subgiant Branch of NGC 1851. *The Astrophysical Journal*, 673:241–250, January 2008.

J. Norris, P. L. Cottrell, K. C. Freeman, and G. S. Da Costa. The abundance spread in the giants of NGC 6752. *Astrophysica Journal*, 244:205–220, February 1981.

P. J. E. Peebles and R. H. Dicke. Origin of the Globular Star Clusters. *Astrophysical Journal*, 154:891, December 1968.

A. C. Phillips. *The Physics of Stars, 2nd Edition*. July 1999.

C. A. Pilachowski. The chemical composition of globular clusters - Global trends. *Astrophysical Journal*, 281:614–623, June 1984.

G. Piotto, L. R. Bedin, J. Anderson, I. R. King, S. Cassisi, A. P. Milone, S. Villanova, A. Pietrinferni, and A. Renzini. A Triple Main Sequence in the Globular Cluster NGC 2808. *The Astrophysical Journal*, 661:L53–L56, May 2007.

S. V. Ramírez and J. G. Cohen. Abundances in Stars from the Red Giant Branch Tip to near the Main-Sequence Turnoff in M5. *AJ*, 125:224–245, January 2003.

M. D. Shetrone. MG and AL Abundances in Halo Globular Clusters. In H. L. Morrison and A. Sarajedini, editors, *Formation of the Galactic Halo...Inside and Out*, volume 92 of *Astronomical Society of the Pacific Conference Series*, page 383, April 1996.

C. Sneden, J. Bean, I. Ivans, S. Lucatello, and J. Sobeck. MOOG: LTE line analysis and spectrum synthesis. Astrophysics Source Code Library, February 2012.

D. N. Spergel. Evacuation of gas from globular clusters by winds from millisecond pulsars. *Nature*, 352:221, July 1991.

N. Suntzeff. The Chemical Homogeneity of Stars in Galactic Globular Clusters. In G. H. Smith and J. P. Brodie, editors, *The Globular Cluster-Galaxy Connection*, volume 48 of *Astronomical Society of the Pacific Conference Series*, page 167, January 1993.

Y. Takeda, M. Ohkubo, and K. Sadakane. Spectroscopic Determination of Atmospheric Parameters of Solar-Type Stars: Description of the Method and Application to the Sun. *PASJ*, 54:451–462, June 2002.

E. Valenti, F. R. Ferraro, S. Perina, and L. Origlia. Near-IR photometry of five Galactic Globular Clusters. *A&A*, 419:139–147, May 2004.

N. Viaux, M. Catelan, G. G. Raffelt, J. Redondo, and A. A. R. Valcarce. The galactic globular cluster M5 (NGC 5904) as a particle physics laboratory. In *European Physical Journal Web of Conferences*, volume 43 of *European Physical Journal Web of Conferences*, page 2004, March 2013.

D. Yong, A. I. Karakas, D. L. Lambert, A. Chieffi, and M. Limongi. Heavy Element Abundances in Giant Stars of the Globular Clusters M4 and M5. *The Astrophysical Journal*, 689:1031–1043, December 2008.

H. Zinnecker, C. J. Keable, J. S. Dunlop, R. D. Cannon, and W. K. Griffiths. The Nuclei of Nucleated Dwarf Elliptical Galaxies - are they Globular Clusters? In J. E. Grindlay and A. G. D. Philip, editors, *The Harlow-Shapley Symposium on Globular Cluster Systems in Galaxies*, volume 126 of *IAU Symposium*, page 603, 1988.